PHYSICAL REVIEW D **84,** 124052 (2011)

# Inspiral-merger-ringdown multipolar waveforms of nonspinning black-hole binaries using the effective-one-body formalism

Yi Pan,[1] Alessandra Buonanno,[1] Michael Boyle,[2] Luisa T. Buchman,[3] Lawrence E. Kidder,[2] Harald P. Pfeiffer,[4] and Mark A. Scheel[3]

[1]*Maryland Center for Fundamental Physics & Joint Space-Science Institute, Department of Physics, University of Maryland, College Park, Maryland 20742, USA*

[2]*Center for Radiophysics and Space Research, Cornell University, Ithaca, New York 14853, USA*

[3]*Theoretical Astrophysics 130-33, California Institute of Technology, Pasadena, California 91125, USA*

[4]*Canadian Institute for Theoretical Astrophysics, 60 St. George Street, University of Toronto, Toronto, Ontario M5S 3H8, Canada*

(Received 22 June 2011; published 27 December 2011)

We calibrate an effective-one-body (EOB) model to numerical-relativity simulations of mass ratios 1, 2, 3, 4, and 6, by maximizing phase and amplitude agreement of the leading (2, 2) mode and of the subleading modes (2, 1), (3, 3), (4, 4) and (5, 5). Aligning the calibrated EOB waveforms and the numerical waveforms at low frequency, the phase difference of the (2, 2) mode between model and numerical simulation remains below $\sim 0.1$ rad throughout the evolution for all mass ratios considered. The fractional amplitude difference at peak amplitude of the (2, 2) mode is 2% and grows to 12% during the ringdown. Using the Advanced LIGO noise curve we study the effectualness and measurement accuracy of the EOB model, and stress the relevance of modeling the higher-order modes for parameter estimation. We find that the effectualness, measured by the mismatch between the EOB and numerical-relativity polarizations which include only the (2, 2) mode, is smaller than 0.2% for binaries with total mass 20–200$M_\odot$ and mass ratios 1, 2, 3, 4, and 6. When numerical-relativity polarizations contain the strongest seven modes, and stellar-mass black holes with masses less than $50M_\odot$ are considered, the mismatch for mass ratio 6 (1) can be as high as 7% (0.2%) when only the EOB (2, 2) mode is included, and an upper bound of the mismatch is 0.5% (0.07%) when all the four subleading EOB modes calibrated in this paper are taken into account. For binaries with intermediate-mass black holes with masses greater than $50M_\odot$ the mismatches are larger. We also determine for which signal-to-noise ratios the EOB model developed here can be used to measure binary parameters with systematic biases smaller than statistical errors due to detector noise.

DOI: 10.1103/PhysRevD.84.124052 PACS numbers: 04.25.D−, 04.25.dg, 04.25.Nx, 04.30.−w

## I. INTRODUCTION

Binary systems composed of black holes and/or neutron stars, spiraling in toward each other and losing energy through the emission of gravitational waves, are among the most promising detectable sources of gravitational waves with the Laser Interferometer Gravitational-wave Observatory (LIGO) [1], Virgo [2], GEO [3], the Large Cryogenic Gravitational Telescope (LCGT) [4], and future space-based detectors. The detectors' noise level and the weakness of the waves prevent observing the waveforms directly. For this reason the search for gravitational waves from binary systems and the extraction of parameters, such as the masses and spins, are based on the matched-filtering technique, which requires accurate knowledge of the waveform of the incoming signal.

The post-Newtonian (PN) expansion is the most powerful approximation scheme in analytical relativity capable of describing the two-body dynamics and gravitational-wave emission of inspiraling compact binary systems [5–8]. The PN approach expands the Einstein equations in the ratio of the characteristic velocity of the binary $v$ to the speed of light or the characteristic size of the compact body to the relative distance between the two bodies. However, as the bodies approach each other towards merger, we expect the PN expansion to lose accuracy because the velocity of the bodies approaches the speed of light, and the relative distance becomes comparable to the size of the compact body. The difficulty in analytically solving the Einstein equations in the merger regime lies mainly in its nonlinear structure. Solving the Einstein equations numerically overcomes this problem.

Prior to the numerical-relativity breakthroughs [9–11], a new and unique method was proposed in analytical relativity to describe the dynamics and gravitational-wave emission of binary black holes during inspiral, merger and ringdown: the effective-one-body (EOB) approach [12–16]. This approach uses the very accurate results of PN theory. However, it does not use those results in their original Taylor-expanded form (i.e., as polynomials in $v/c$), but instead in some appropriate resummed form. In particular, the effective-one-body approach [12,14,15,17,18] maps the dynamics of two compact objects of masses $m_1$ and $m_2$, and spins $\mathbf{S}_1$ and $\mathbf{S}_2$, into the dynamics of one test particle of mass $\mu = m_1 m_2/(m_1 + m_2)$ and spin $\mathbf{S}_*$ moving in a deformed Kerr metric

 

with mass $M = m_1 + m_2$ and spin $\mathbf{S}_{\rm Kerr}$. The deformation parameter is the symmetric mass ratio $m_1 m_2/(m_1 + m_2)^2$ which ranges between 0 (test-particle limit) and 1/4 (equal-mass limit). The other crucial aspect of the EOB approach is the way it builds the full waveform, including merger and ringdown. The EOB approach assumes that the merger is very short in time, although broad in frequency, and builds the merger-ringdown signal by attaching to the plunge signal a superposition of quasinormal modes. This match happens at the EOB light ring (or photon orbit) where the peak of the potential barrier around the merged black hole sits.

The analyses and theoretical progress made in Refs. [18–32] have demonstrated that it is possible to devise and calibrate analytical EOB waveforms for use in detection searches. This is crucial, since thousands of waveform templates need to be computed to extract the signal from the noise, an impossible demand for numerical relativity alone. For example, the EOB waveforms calibrated to numerical-relativity waveforms in Ref. [20] have been used in LIGO and Virgo to search for the first time for high-mass merging black holes [33].

This paper is a step forward in building more faithful EOB waveforms to be used for detection and parameter estimation. We calibrate the EOB model to accurate numerical-relativity simulations of mass ratios 1, 2, 3, 4, and 6, so that the phase and amplitude agreement of the leading (2, 2) mode and also the subleading modes (2, 1), (3, 3), (4, 4) and (5, 5) are minimized throughout inspiral, merger and ringdown. The numerical simulations are produced by the pseudospectral code SPEC of the Caltech-Cornell-CITA collaboration [34–40] (see particularly Ref. [41] for details). The waveforms are extracted as Regge-Wheeler-Zerilli data [42], and extrapolated to infinite extraction radius [43]. Since the numerical-relativity modes satisfy the relation $h_{\ell m} = (-1)^\ell h^*_{\ell -m}$ with high accuracy, where $*$ denotes complex conjugate, we assume its validity also for the analytical modes. As a consequence, any statement in the paper concerning an $(\ell, m)$ mode automatically holds for its complex conjugate $(\ell, -m)$ mode. We find that the (3, 2) mode has a distinct feature that currently cannot be accounted for with the EOB model used in this paper. Moreover, we find that the (6, 6) mode (and very likely other modes with $m = \ell$) can be calibrated in the same way as the (4, 4) and (5, 5) modes. However, we do not consider the (6, 6) mode since, for the range of mass ratios considered here, its amplitude is much lower than the other subleading-mode amplitude, and therefore contributes little to the full polarization waveforms.

The paper is organized as follows. In Sec. II, we describe the EOB dynamics, the waveforms and its adjustable parameters. In Sec. III we discuss the numerical-relativity simulations produced by the pseudospectral code SPEC [41] and estimate the phase and amplitude errors. Then, we calibrate EOB to numerical-relativity modes and discuss its effectualness and measurement accuracy when searching for gravitational waves with Advanced LIGO detectors. In Sec. V we compare our EOB model and its performance in matching numerical-relativity results to previous work. We summarize our main conclusions in Sec. VI. In Appendix A we discuss some interesting features of the (3, 2) mode. In Appendix B we list several quantities which enter the EOB waveforms and energy flux.

## II. EFFECTIVE-ONE-BODY MODEL

In Secs. II A, II B, and II C (see also Appendix B) we shall discuss in detail all the building blocks of the EOB dynamics and waveforms, and its adjustable parameters. The EOB model used in this paper is presented in a self-contained way to allow readers to reproduce it if desired. We note that many important features of the EOB model have been developed in several papers [12–14,19,20,22,23,27–32,44,45]].

If the EOB model were compared to the numerical-relativity simulations used in this paper *without any calibration*, i.e., at the PN order currently known, 3PN in the conservative dynamics and 3. 5PN in the radiation-reaction sector, we would find at merger a phase difference for the (2, 2) mode of up to 3.6 rad over the mass-ratio range $q = 1, 2, 3, 4, 6$. Moreover, the EOB amplitude would peak around $30M$ before the numerical-relativity peak, with a fractional amplitude difference at the peak of $\sim 8\%$. A straightforward way of reducing the differences is to insert in the dynamics and radiation-reaction force higher-order (pseudo) PN terms (or EOB adjustable parameters) and *calibrate* them to the numerical results. The advantage of the EOB approach is that the dynamics and radiation-reaction force (and modes) are written in a way which isolates the crucial functions that determine the evolution. As we shall see below, these functions are the EOB radial potential $A(r)$, or time-time component of the EOB metric, and some phase and amplitude functions appearing in the EOB (factorized) gravitational modes.

### A. Effective-one-body dynamics

We set $M = m_1 + m_2$, $\mu = m_1 m_2/M = \nu M$, $q = m_1/m_2$, and use natural units $G = c = 1$. The EOB effective metric reads [13]

$$ds^2_{\rm eff} = -A(r)dt^2 + \frac{D(r)}{A(r)}dr^2 + r^2(d\Theta^2 + \sin^2\Theta d\Phi^2), \tag{1}$$

where we use dimensionless polar coordinates $(r, \Phi)$ and their conjugate momenta $(p_r, p_\Phi)$. Replacing the radial momentum $p_r$ with $p_{r_*}$ which is the conjugate momentum to the EOB *tortoise* radial coordinate $r_*$,

$$\frac{dr_*}{dr} = \frac{\sqrt{D(r)}}{A(r)}, \tag{2}$$

we obtain the EOB effective Hamiltonian [13,14,46]

$$H^{\rm eff}(r, p_{r_*}, p_\Phi) \equiv \mu \hat{H}^{\rm real}(r, p_{r_*}, p_\Phi) = \mu \sqrt{p^2_{r_*} + A(r)\left[1 + \frac{p^2_\Phi}{r^2} + 2(4-3\nu)\nu \frac{p^4_{r_*}}{r^2}\right]}, \tag{3}$$

where we have neglected the factor $D(r)^2/A(r)^4$ in front of the term $p^4_{r_*}$ which would introduce PN terms higher than 3PN order, but more importantly would cause the EOB gravitational frequency to grow too quickly near merger.

The real EOB Hamiltonian reads [13]

$$H^{\rm real}(r, p_{r_*}, p_\Phi) \equiv \mu \hat{H}^{\rm real}(r, p_{r_*}, p_\Phi) = M\sqrt{1 + 2\nu\left(\frac{H^{\rm eff} - \mu}{\mu}\right)} - M. \tag{4}$$

The Taylor approximants to the coefficients $A(r)$ and $D(r)$ can be written as [13,14]

$$A_k(r) = \sum_{i=0}^{k+1} \frac{a_i(\nu)}{r^i}, \qquad D_k(r) = \sum_{i=0}^{k} \frac{d_i(\nu)}{r^i}. \tag{5}$$

The functions $A(r)$, $D(r)$, $A_k(r)$ and $D_k(r)$ all depend on the symmetric mass ratio $\nu$ through the $\nu$-dependent coefficients $a_i(\nu)$ and $d_i(\nu)$ [see Eqs. (47) and (48) in Ref. [22]]. The functions $A_k(r)$ and $D_k(r)$ are currently known through 3PN order, i.e., $k = 3$. During the last stages of inspiral and plunge, the EOB dynamics can be adjusted closer to the numerical simulations by including in the radial potential $A(r)$ a few adjustable parameters of the EOB dynamics. Notably, the 4PN coefficient $a_5(\nu)$ [20,22,23,27–29,44] and even the 5PN coefficient $a_6(\nu)$ [31].[1]

To enforce the presence of the EOB innermost stable circular orbit (ISCO), Ref. [14] suggested using the Padé expansion of the function $A(r)$. For $A(r)$ we employ the Padé expression $A^1_5(r)$ at 5PN order, while for $D(r)$ we use the Padé expression $D^0_3(r)$ at 3PN order. We could also introduce EOB adjustable parameters at 4PN and 5PN order in $D(r)$, say $d_4(\nu)$ and $d_5(\nu)$. However, this modification would affect mainly the radial motion [see Eq. (10a) below] which becomes important only at the very end of the evolution. For the EOB model developed in this paper we find that these other adjustable parameters are not needed. The quantity $D^0_3(r)$ reads

$$D^0_3(r) = \frac{r^3}{(52\nu - 6\nu^2) + 6\nu r + r^3}, \tag{6}$$

while $A^1_5(r)$ reads

$$A^1_5(r) = \frac{\mathrm{Num}(A^1_5)}{\mathrm{Den}(A^1_5)}, \tag{7}$$

with

$$\mathrm{Num}(A^1_5) = r^4[-64 + 12a_4 + 4a_5 + a_6 + 64\nu - 4\nu^2] + r^5[32 - 4a_4 - a_5 - 24\nu], \tag{8}$$

and

$$\mathrm{Den}(A^1_5) = 4a_4^2 + 4a_4a_5 + a_5^2 - a_4a_6 + 16a_6 + (32a_4 + 16a_5 - 8a_6)\nu + 4a_4\nu^2 + 32\nu^3 + r[4a_4^2 + a_4a_5 + 16a_5 + 8a_6 + (32a_4 - 2a_6)\nu + 32\nu^2 + 8\nu^3] + r^2[16a_4 + 8a_5 + 4a_6 + (8a_4 + 2a_5)\nu + 32\nu^2] + r^3[8a_4 + 4a_5 + 2a_6 + 32\nu - 8\nu^2] + r^4[4a_4 + 2a_5 + a_6 + 16\nu - 4\nu^2] + r^5[32 - 4a_4 - a_5 - 24\nu], \tag{9}$$

where $a_4 = [94/3 - (41/32)\pi^2]\nu$ and to ease the notation we have omitted the $\nu$ dependence of $a_5$ and $a_6$ in the expressions above. The quantities $a_5$ and $a_6$ are the adjustable parameters of the EOB dynamics [23] (see Table I). They will be determined below when calibrating the EOB to numerical-relativity waveforms. Their explicit expressions are given in Eq. (36).

The EOB Hamilton equations are written in terms of the reduced, i.e., dimensionless quantities $\hat{H}^{\rm real}$ [defined in Eq. (4)] [12]. They read[2]

TABLE I. Summary of adjustable parameters of the EOB model considered in this paper. We notice that to calibrate the EOB (2, 2) mode, we *only* need $a_5$, $a_6$ and $\Delta t^{22}_{\rm match}$. To calibrate each subleading mode (2, 1), (3, 3), (4, 4), and (5, 5), we need four adjustable parameters. The values of the adjustable parameters used in this paper are given in Eqs. (36) to (39) and (41).

| EOB dynamics adjustable parameters | EOB waveform adjustable parameters |
|---|---|
| $a_5$, $a_6$ | $\Delta t^{\ell m}_{\rm match}$ |
| | $\rho^{(p)}_{\ell m}$ |
| | $\delta^{(q)}_{\ell m}$ |
| | $\omega^{\rm pQNM}_{\ell m}$ |

[1]The radial potential $A(r)$ may contain logarithmic terms at 4PN and 5PN orders [47,48] which we do not try to model here.

[2]We notice that the second term on the right-hand side of Eq. (10c) is generated when taking the nonspinning limit of the spinning EOB model of Ref. [16]

$$\frac{dr}{d\hat{t}} = \frac{A_5^1(r)}{\sqrt{D_3^0(r)}} \frac{\partial \hat{H}^{\rm real}}{\partial p_{r_*}}(r, p_{r_*}, p_\Phi), \tag{10a}$$

$$\frac{d\Phi}{d\hat{t}} = \frac{\partial \hat{H}^{\rm real}}{\partial p_\Phi}(r, p_{r_*}, p_\Phi), \tag{10b}$$

$$\frac{dp_{r_*}}{d\hat{t}} = -\frac{A_5^1(r)}{\sqrt{D_3^0(r)}} \frac{\partial \hat{H}^{\rm real}}{\partial r}(r, p_{r_*}, p_\Phi) + {}^{\rm nK}\hat{\mathcal{F}}_\Phi \frac{p_{r_*}}{p_\Phi}, \tag{10c}$$

$$\frac{dp_\Phi}{d\hat{t}} = {}^{\rm nK}\hat{\mathcal{F}}_\Phi, \tag{10d}$$

with the definition $\hat{\Omega} \equiv d\Phi/d\hat{t} \equiv M\Omega$. The initial conditions for the EOB Hamilton equations will be discussed in Sec. II D. Furthermore, for the $\Phi$ component of the radiation-reaction force we use a non-Keplerian radiation-reaction force[3]

$${}^{\rm nK}\hat{\mathcal{F}}_\Phi = -\frac{1}{\nu v_\Omega^3}\frac{dE}{dt}, \tag{11}$$

where $v_\Omega \equiv \hat{\Omega}^{1/3}$, and $dE/dt$ is the gravitational-wave energy flux for quasicircular orbits obtained by summing over the gravitational-wave modes $(l, m)$. We use

$$\frac{dE}{dt} = \frac{v_\Omega^6}{8\pi}\sum_{\ell=2}^{7}\sum_{m=\ell-2}^{\ell} m^2 \left|\frac{\mathcal{R}}{M}h_{\ell m}\right|^2. \tag{12}$$

Note that because $|h_{\ell,m}| = |h_{\ell,-m}|$, we extend the sum over positive $m$ modes only. Moreover, for the cases studied in this paper, including more modes in the summation has a negligible effect on the energy flux. Specifically, if we sum $\ell$ through $\ell = 8$ and sum $m = 0, \ldots, \ell$, the gravitational-wave phase of the EOB (2, 2) mode changes by less than 0.01 rad at merger, which is negligible compared to the phase error of numerical-relativity modes. We find that the dominant computational cost in generating the EOB waveforms is the calculation of the energy flux. The choice of modes ($\ell$, $m$ in Eq. (12) saves us about a third of the computational time when compared to the case where the sum extends up to $\ell = 8$, and runs over $m = 0, \ldots, \ell$. The explicit expression of the modes $h_{\ell m}$ is given below, in Secs. II B and II C.

### B. EOB waveform: inspiral and plunge

Having described the inspiral and plunge dynamics, we now turn to the gravitational-wave modes $h_{\ell m}$. The latter can be employed to compute consistently the inspiral dynamics through the radiation-reaction force [31] [see Eq. (12)]. The inspiral and plunge EOB modes are given by

$$h_{\ell m}^{\rm insp-plunge} = h_{\ell m}^{\rm F} N_{\ell m}, \tag{13}$$

where the $N_{\ell m}$ describe effects that go beyond the quasicircular assumption and will be defined below [see Eq. (22)], and the $h_{\ell m}^{\rm F}$ are the factorized resummed modes. In the nonspinning case, Refs. [23,31] have shown that the resummed, factorized modes proposed in Ref. [30] are in excellent agreement with the numerical waveforms [29,34]. We have [30],

$$h_{\ell m}^{\rm F} = h_{\ell m}^{(N,\epsilon)} \hat{S}_{\rm eff}^{(\epsilon)} T_{\ell m} e^{i\delta_{\ell m}} (\rho_{\ell m})^\ell, \tag{14}$$

where $\epsilon$ denotes the parity of the multipolar waveform.

$$\epsilon = \begin{cases} 0, & \ell + m \text{ is even} \\ 1, & \ell + m \text{ is odd} \end{cases}. \tag{15}$$

The leading term in Eq. (14), $h_{\ell m}^{(N,\epsilon)}$, is the Newtonian contribution

$$h_{\ell m}^{(N,\epsilon)} = \frac{M\nu}{\mathcal{R}} n_{\ell m}^{(\epsilon)} c_{\ell+\epsilon}(\nu) V_\Phi^\ell Y^{\ell-\epsilon,-m}\left(\frac{\pi}{2}, \Phi\right), \tag{16}$$

where $\mathcal{R}$ is the distance from the source; the $Y^{\ell m}(\Theta, \Phi)$ are the scalar spherical harmonics; the functions $n_{\ell m}^{(\epsilon)}$ and $c_{\ell+\epsilon}(\nu)$ are explicitly given in Appendix B [see Eqs. (B7) and (B8)]. Moreover, for reasons that will be explained in Sec. III E, we choose

$$V_\Phi^\ell = v_\Phi^{(\ell+\epsilon)} \qquad (\ell, m) \neq (2, 1), (4, 4), \tag{17a}$$

$$V_\Phi^\ell = \frac{1}{r_\Omega} v_\Phi^{(\ell+\epsilon-2)} \qquad (\ell, m) = (2, 1), (4, 4); \tag{17b}$$

with $v_\Phi$ and $r_\Omega$ defined by [22]

$$v_\Phi \equiv \hat{\Omega} r_\Omega \equiv \hat{\Omega} r[\psi(r, p_\Phi)]^{1/3} \tag{18}$$

and

$$\psi(r, p_\Phi) = \frac{2\left\{1 + 2\nu\left[\sqrt{A_5^1(r)(1 + p_\Phi^2/r^2)} - 1\right]\right\}}{r^2 dA_5^1(r)/dr}. \tag{19}$$

The quantity $p_\Phi$ in the above equation is the dynamical $p_\Phi$ being used in the evolution, contrary to the choice made in Ref. [22] where $p_\Phi$ was chosen to satisfy the circular-orbit condition. The function $\hat{S}_{\rm eff}^{(\epsilon)}$ in Eq. (14) is an effective source term that in the circular-motion limit contains a pole at the EOB light ring. It is given in terms of the EOB dynamics as

$$\hat{S}_{\rm eff}^{(\epsilon)}(r, p_{r_*}, p_\Phi) = \begin{cases} \hat{H}^{\rm eff}(r, p_{r_*}, p_\Phi), & \epsilon = 0, \\ \hat{L}_{\rm eff} = p_\Phi v_\Omega, & \epsilon = 1, \end{cases} \tag{20}$$

where $\hat{H}^{\rm eff}(r, p_{r_*}, p_\Phi)$ can be read from Eq. (3). The factor $T_{\ell m}$ in Eq. (14) resums the leading-order logarithms of tail effects, it reads

[3]Note that Eq. (11) is only *implicitly* non-Keplerian, in contrast to similar expressions in other papers which explicitly introduce non-Keplerian terms. In this case, the non-Keplerian behavior is hidden in the wave amplitudes $h_{\ell m}$, as described in the following section.

$$T_{\ell m} = \frac{\Gamma(\ell + 1 - 2imH^{\rm real}\Omega)}{\Gamma(\ell+1)} \exp[\pi m \Omega H^{\rm real}] \times \exp[2im\Omega H^{\rm real} \log(2m\Omega r_0)], \quad (21)$$

where $r_0 = 2\exp(-1/2)M$ [26] and $H^{\rm real}$ can be read from Eq. (4).

The factor $e^{i\delta_{\ell m}}$ in Eq. (14) is a phase correction due to subleading-order logarithms, while the factor $(\rho_{\ell m})^\ell$ in Eq. (14) collects the remaining PN terms. The full expressions for $\delta_{\ell m}$ and $\rho_{\ell m}$ are given in Appendix B. To improve the agreement with the numerical-relativity higher modes, we introduce and calibrate in $\delta_{\ell m}$ and $\rho_{\ell m}$ a few higher-order, yet unknown, PN terms (see also Refs. [49,50]). Details of this are given below [see Eqs. (38) and (39)], so here we merely remark that in the spirit of Ref. [23], those coefficients should be considered adjustable parameters of the EOB waveform (see Table I). The introduction of these higher-order PN terms in the modes $\neq (2,2)$ is not surprising, because these modes are known at lower PN order than the (2, 2) mode. We note that the adjustable parameters in $\delta_{\ell m}$ and $\rho_{\ell m}$ will be used only to improve the agreement between the EOB and numerical-relativity modes. They will not be included in the energy flux entering the dynamics through Eq. (12).

Finally, the function $N_{\ell m}$ entering Eq. (13) reads

$$N_{\ell m} = \left[1 + \frac{p_{r^*}^2}{(r\hat{\Omega})^2}\left(a_1^{h_{\ell m}} + \frac{a_2^{h_{\ell m}}}{r} + \frac{a_3^{h_{\ell m}}}{r^{3/2}}\right)\right] \times \exp\left[i\left(b_1^{h_{\ell m}}\frac{p_{r^*}}{r\hat{\Omega}} + b_2^{h_{\ell m}}\frac{p_{r^*}^3}{r\hat{\Omega}}\right)\right], \quad (22)$$

where the quantities $a_i^{h_{\ell m}}$ and $b_i^{h_{\ell m}}$ are the non-quasicircular (NQC) orbit coefficients [23,25,27–29,32,45].

To better understand how we fix the parameters $a_i^{h_{\ell m}}$ and $b_i^{h_{\ell m}}$, we plot in Fig. 1 the amplitudes of the dominant numerical $h_{\ell m}$. As already observed in Refs. [20,32,51–53], the peaks of the modes occur at different times. In Fig. 1 we have indicated these times relative to the peak of $h_{22}$. Our goal is to model the EOB modes, through the parameters $a_i^{h_{\ell m}}$ and $b_i^{h_{\ell m}}$, in such a way to (i) reproduce the *shape* of the numerical-relativity amplitudes close to the peak, and (ii) preserve the time differences between the modes.

So, for each mode, we fix the three parameters $a_i^{h_{\ell m}}$ in the amplitude and the two coefficients $b_i^{h_{\ell m}}$ in the phase by requiring that the peaks of the numerical and EOB $h_{\ell m}$, as well as their frequencies at the peaks, coincide.[4]

[4]During the course of this work we noticed that Ref. [32] had independently developed the same procedure of us in fixing the NQC phase coefficients using $\omega_{\ell m}^{\rm NR}$ and $\dot{\omega}_{\ell m}^{\rm NR}$. However, Ref. [32] computes those numerical quantities at the light-ring position $3M$ instead of the peak of the $(\ell, m)$ modes as we do. Reference [32] focused on the EOB modeling in the extreme mass-ratio limit.

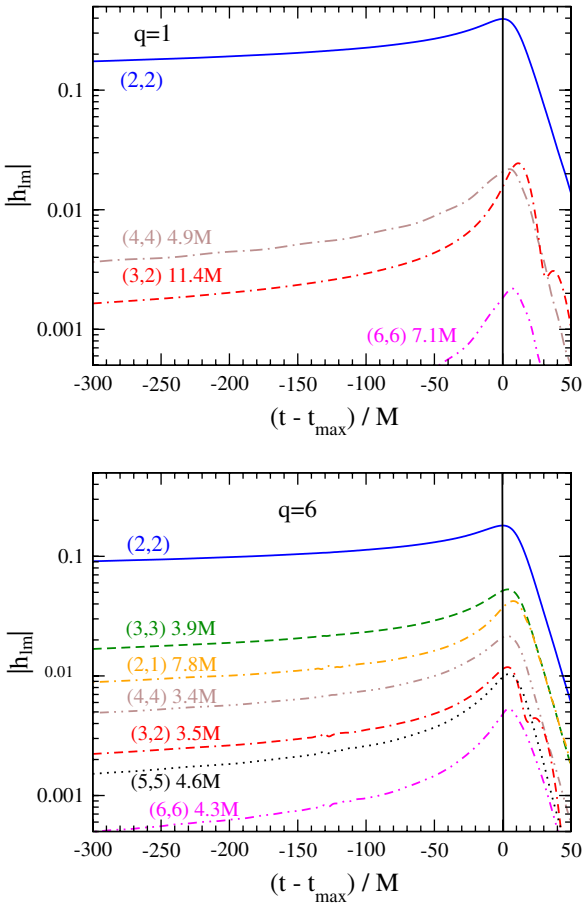


FIG. 1 (color online). Amplitude of extrapolated numerical-relativity waveforms for the dominant modes. The two panels from top to bottom are for mass ratios $q = 1$ and $q = 6$, respectively. Each curve is labeled with its respective $(l, m)$ mode, and the time-delay $\Delta t_{\rm peak}^{\ell m}$ between the extrema of $|h_{22}|$ and $|h_{lm}|$. The horizontal axis measures the time-difference to the peak of $|h_{22}|$.

Specifically, we impose five conditions listed below for each mode.

(1) The time at which the EOB $h_{22}$ reaches its peak should coincide with the time at which the EOB orbital frequency $\Omega$ reaches its peak. We denote this time with $t_{\rm peak}^{\Omega}$. It was observed [23,26,31] that, once the EOB and numerical phases are aligned at low frequency and calibrated, the time at which the numerical $h_{22}$ reaches its peak coincides with the EOB light-ring time. Moreover, the latter occurs immediately ($< 1M$ in time) after the peak of $\Omega$. The peaks of higher-order numerical modes differ from the peak of the numerical $h_{22}$ mode by a few $M$ in time. We define this time difference as

$$\Delta t_{\rm peak}^{\ell m} = t_{\rm peak}^{\ell m} - t_{\rm peak}^{22} = t_{d|h_{\ell m}^{\rm NR}|/dt=0} - t_{d|h_{22}^{\rm NR}|/dt=0}, \quad (23)$$

and require that the peaks of the EOB $h_{\ell m}$ occur at the time $t^{\Omega}_{\rm peak} + \Delta t^{\ell m}_{\rm peak}$.

(2) The peak of the EOB $h_{\ell m}$ should have the same amplitude as the peak of the numerical $h_{\ell m}$, that is,

$$|h^{\rm EOB}_{\ell m}(t^{\Omega}_{\rm peak} + \Delta t^{\ell m}_{\rm peak})| = |h^{\rm NR}_{\ell m}(t^{\ell m}_{\rm peak})|. \quad (24)$$

(3) The peak of the EOB $h_{\ell m}$ should have the same second time derivative as the peak of the numerical $h_{\ell m}$, that is,

$$\frac{d^2|h^{\rm EOB}_{\ell m}|}{dt^2}\bigg|_{t^{\Omega}_{\rm peak}+\Delta t^{\ell m}_{\rm peak}} = \frac{d^2|h^{\rm NR}_{\ell m}|}{dt^2}\bigg|_{t^{\ell m}_{\rm peak}}. \quad (25)$$

This condition guarantees that the local extremum of $|h^{\rm EOB}_{\ell m}|$ at $t = t^{\Omega}_{\rm peak} + \Delta t^{\ell m}_{\rm peak}$ is a local maximum.

(4) The frequency of the numerical and EOB $h_{\ell m}$ waveforms should coincide at their peaks, that is,

$$\omega^{\rm EOB}_{\ell m}(t^{\Omega}_{\rm peak} + \Delta t^{\ell m}_{\rm peak}) = \omega^{\rm NR}_{\ell m}(t^{\ell m}_{\rm peak}) \quad (26)$$

(5) The time derivative of the frequency of the numerical and EOB $h_{\ell m}$ waveforms should coincide at their peaks, that is,

$$\dot{\omega}^{\rm EOB}_{\ell m}(t^{\Omega}_{\rm peak} + \Delta t^{\ell m}_{\rm peak}) = \dot{\omega}^{\rm NR}_{\ell m}(t^{\ell m}_{\rm peak}) \quad (27)$$

In Sec. III A we shall find that the functions $\Delta t^{\ell m}_{\rm peak}$, $|h^{\rm NR}_{\ell m}(t^{\ell m}_{\rm peak})|$, $d^2|h^{\rm NR}_{\ell m}|/dt^2|_{t^{\ell m}_{\rm peak}}$, $\omega^{\rm NR}_{\ell m}(t^{\ell m}_{\rm peak})$, and $\dot{\omega}^{\rm NR}_{\ell m}(t^{\ell m}_{\rm peak})$ are reasonably approximated by smooth functions of $\nu$ (see Table II).

The NQC coefficients $a^{h_{\ell m}}_i$ are calculated within the EOB model using the fitting formulas in Table II. The calculation involves a computationally expensive iterative procedure. Basically, in each round of the iteration, $a^{h_{\ell m}}_i$ and $b^{h_{\ell m}}_i$ are calculated to satisfy the five conditions listed above. The amplitude corrections $a^{h_{\ell m}}_i$ then enter the dynamics through the energy flux given in Eq. (12). The new EOB dynamics generate new modes and, thus, new $a^{h_{\ell m}}_i$. We stop the iteration when $a^{h_{\ell m}}_i$ converge on successive runs. In this paper, for technical convenience, we include *only* $a^{h_{22}}_i(\nu)$ in the energy flux (12) and ignore the effect of higher-order-mode NQC corrections on the inspiral dynamics. However, we do include the higher-order-mode NQC corrections when building the EOB waveforms and compare them to the numerical-relativity ones. Neglecting higher-order-mode NQC corrections in the energy flux (12) is insignificant for three reasons: The higher-order-mode contribution to the energy flux is about an order of magnitude smaller than that of the dominant (2, 2) mode; the NQC corrections in the amplitude are a relatively small correction, typically ~10% at merger; and the NQC correction is most important close to merger where the radiation reaction has little effect on the plunging dynamics.

TABLE II. We list in the third column $\nu$-fits of $\Delta t^{\ell m}_{\rm peak}$, $|h^{\rm NR}_{\ell m}(t^{\ell m}_{\rm peak})|$, $d^2|h^{\rm NR}_{\ell m}|/dt^2|_{t^{\ell m}_{\rm peak}}$, $\omega^{\rm NR}_{\ell m}(t^{\ell m}_{\rm peak})$, and $\dot{\omega}^{\rm NR}_{\ell m}(t^{\ell m}_{\rm peak})$ against numerical data of mass ratios $q = 1$, 2, 3, 4 and 6 for modes (2, 2), (3, 3), (2, 1), (4, 4) and (5, 5). In the fitting formulas, the relative mass difference is $\delta m \equiv (m_1 - m_2)/(m_1 + m_2) = \sqrt{1 - 4\nu}$.

| | $(\ell, m)$ | Fit formula |
|---|---|---|
| $\Delta t^{\ell m}_{\rm peak}$ | (2, 2) | 0 |
| | (3, 3) | $3.383 + 3.847\nu + 8.979\nu^2$ |
| | (2, 1) | $10.67 - 41.41\nu + 76.1\nu^2$ |
| | (4, 4) | $5.57 - 49.86\nu + 154.3\nu^2$ |
| | (5, 5) | $6.693 - 34.47\nu + 102.7\nu^2$ |
| $\lvert h^{\rm NR}_{\ell m}(t^{\ell m}_{\rm peak})\rvert$ | (2, 2) | $\nu(1.422 + 0.3013\nu + 1.246\nu^2)$ |
| | (3, 3) | $\nu\delta m(0.5761 - 0.09638\nu + 2.715\nu^2)$ |
| | (2, 1) | $\nu\delta m(0.4832 - 0.01032\nu)$ |
| | (4, 4) | $\nu(0.354 - 1.779\nu + 2.834\nu^2)$ |
| | (5, 5) | $\nu\delta m(0.1353 - 0.1485\nu)$ |
| $100 \times \frac{d^2\lvert h^{\rm NR}_{\ell m}\rvert}{dt^2}\big\rvert_{t^{\ell m}_{\rm peak}}$ | (2, 2) | $-\nu(0.1679 + 1.44\nu - 2.001\nu^2)$ |
| | (3, 3) | $-\nu\delta m(0.2518 - 0.8145\nu + 5.731\nu^2)$ |
| | (2, 1) | $-\nu\delta m(0.1867 + 0.6094\nu)$ |
| | (4, 4) | $-\nu(0.1813 - 0.9935\nu + 1.858\nu^2)$ |
| | (5, 5) | $-\nu\delta m(0.09051 - 0.1604\nu)$ |
| $\omega^{\rm NR}_{\ell m}(t^{\ell m}_{\rm peak})$ | (2, 2) | $0.2733 + 0.2316\nu + 0.4463\nu^2$ |
| | (3, 3) | $0.4539 + 0.5376\nu + 1.042\nu^2$ |
| | (2, 1) | $0.2907 - 0.08338\nu + 0.587\nu^2$ |
| | (4, 4) | $0.6435 - 0.05103\nu + 2.216\nu^2$ |
| | (5, 5) | $0.8217 + 0.2346\nu + 2.599\nu^2$ |
| $\dot{\omega}^{\rm NR}_{\ell m}(t^{\ell m}_{\rm peak})$ | (2, 2) | $0.005862 + 0.01506\nu + 0.02625\nu^2$ |
| | (3, 3) | $0.01074 + 0.0293\nu + 0.02066\nu^2$ |
| | (2, 1) | $0.00149 + 0.09197\nu - 0.1909\nu^2$ |
| | (4, 4) | $0.01486 + 0.08529\nu - 0.2174\nu^2$ |
| | (5, 5) | $0.01775 + 0.09801\nu - 0.1686\nu^2$ |

The iterative procedure explained above usually takes four to five iterations to converge, increasing the computational cost to generate an EOB waveform by a similar factor. Therefore, to reduce computational cost, we give fitting formulas of $a^{h_{22}}_i$ in Eq. (40). We shall emphasize however that $a^{h_{22}}_i$ are not adjustable parameters of the EOB model and are not required as inputs to generate the (2, 2) modes.

Finally, to demonstrate the effect of the NQC corrections (22), we show in Fig. 2 the EOB amplitude for the (2, 2) mode without and with NQC corrections, that is, without and with the factor $N_{\ell m}$ in Eq. (13). We notice that for $q = 1$ and $q = 6$, the amplitude without the NQC corrections differs from the numerical one *only* by $-0.23\%$ and $-0.67\%$, at $t = 6.2M$ and $t = 5.7M$ before the peak, respectively. However, even this small difference needs to be removed to minimize the error when attaching the merger-ringdown waveform. The latter will be discussed in the next section.

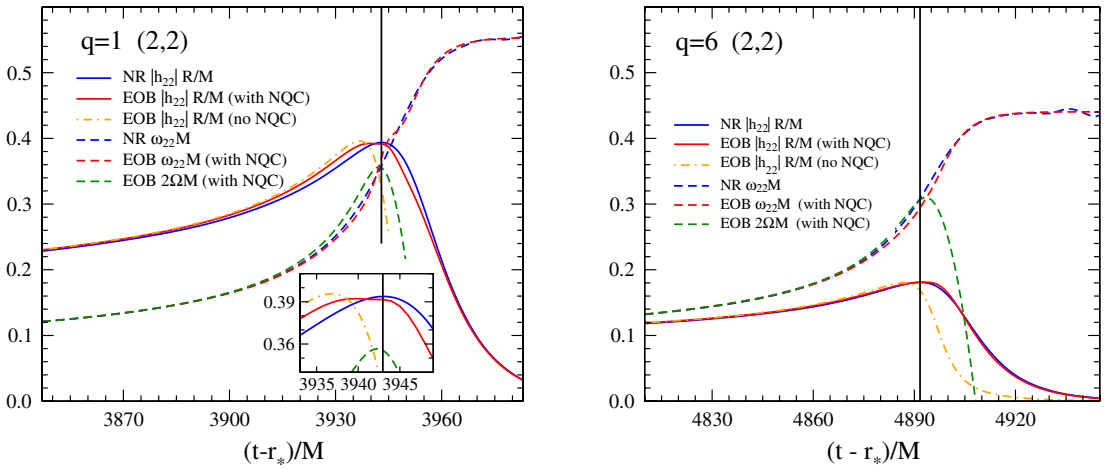


FIG. 2 (color online). We compare the numerical-relativity and EOB $h_{22}$ amplitudes with and without the NQC corrections $N_{\ell m}$ given in Eq. (22). We also plot the numerical and EOB gravitational frequency of the (2, 2) mode and twice the EOB orbital frequency. The left panel refers to $q = 1$ and the right panel to $q = 6$. The horizontal axis is the retarded time in the numerical-relativity simulation. The vertical lines mark the peaks of the numerical-relativity $h_{22}$ amplitudes.

### C. EOB waveform: merger and ringdown

The procedure of building the merger-ringdown waveform in the EOB approach has improved over the years [12,19,20,23,28,29,54]. For each mode $(\ell, m)$ we have

$$h_{\ell m}^{\mathrm{merger-RD}}(t) = \sum_{n=0}^{N-1} A_{\ell mn} e^{-i\sigma_{\ell mn}(t - t_{\mathrm{match}}^{\ell m})}, \tag{28}$$

where $n$ is the overtone number of the Kerr quasinormal mode (QNM), $N$ is the number of overtones included in our model, and $A_{\ell mn}$ are complex amplitudes to be determined by a matching procedure described below. The quantity $\sigma_{\ell mn} = \omega_{\ell mn} - i/\tau_{\ell mn}$, where the oscillation frequencies $\omega_{\ell mn} > 0$ and the decay times $\tau_{\ell mn} > 0$, are numbers associated with each QNM. The complex frequencies are known functions of the final black-hole mass and spin and can be found in Ref. [55].

In this paper we model the ringdown modes as a linear combination of eight QNMs, i.e., $N = 8$. Mass and spin of the final black hole $M_f$ and $a_f$ are computed from numerical data for mass ratios $q = 1$, 2, 3, 4 and 6. Notably, we employ the fitting formula obtained by fitting the numerical results of $M_f$ and $a_f$

$$\frac{M_f}{M} = 1 + \left(\sqrt{\frac{8}{9}} - 1\right)\nu - 0.4333\nu^2 - 0.4392\nu^3, \tag{29a}$$

$$\frac{a_f}{M_f} = \sqrt{12}\nu - 3.871\nu^2 + 4.028\nu^3. \tag{29b}$$

The above formula differs from the analogous fitting formula given in Ref. [20] by $<0.3\%$ in $M_f$ and $<2\%$ in $a_f$, because of the more accurate numerical data used here.

The complex amplitudes $A_{\ell mn}$ in Eq. (28) are determined by matching the EOB merger-ringdown waveform (28) with the EOB inspiral-plunge waveform (13). In order to do this, $N$ independent complex equations are needed. In Ref. [23] we introduced the hybrid-comb matching in which $N$ equations are obtained at $N - 4$ points evenly sampled in a small time interval $\Delta t_{\mathrm{match}}^{\ell m}$ ended at $t_{\mathrm{match}}^{\ell m}$, and we imposed the condition that the inspiral-plunge and merger-ringdown waveforms coincide at the $N - 4$ points and their first- and second-order time derivatives coincide at the first and the last points. Unlike in Ref. [23], we no longer demand second-order time derivatives of the waveforms to coincide anywhere in order to improve the numerical stability of the matching procedure. Instead, we impose equality of the waveform at $N - 2$ points evenly sampled from $t_{\mathrm{match}}^{\ell m} - \Delta t_{\mathrm{match}}^{\ell m}$ to $t_{\mathrm{match}}^{\ell m}$, and we require continuity of the first-time derivative of the waveforms at $t_{\mathrm{match}}^{\ell m} - \Delta t_{\mathrm{match}}^{\ell m}$ and $t_{\mathrm{match}}^{\ell m}$, i.e.,

$$h_{\ell m}^{\mathrm{insp-plunge}}\left(t_{\mathrm{match}}^{\ell m} - \frac{k}{N-3}\Delta t_{\mathrm{match}}^{\ell m}\right) = h_{\ell m}^{\mathrm{merger-RD}}\left(t_{\mathrm{match}}^{\ell m} - \frac{k}{N-3}\Delta t_{\mathrm{match}}^{\ell m}\right), \tag{30}$$

$$(k = 0, 1, 2, \ldots, N-3),$$

and

$$\dot{h}_{\ell m}^{\mathrm{insp-plunge}}\left(t_{\mathrm{match}}^{\ell m} - \frac{k}{N-3}\Delta t_{\mathrm{match}}^{\ell m}\right) = \dot{h}_{\ell m}^{\mathrm{merger-RD}}\left(t_{\mathrm{match}}^{\ell m} - \frac{k}{N-3}\Delta t_{\mathrm{match}}^{\ell m}\right), \tag{31}$$

$$(k = 0 \quad \text{and} \quad N-3),$$

The matching time $t_{\mathrm{match}}^{\ell m}$ is fixed to be the peak of the EOB $h_{\ell m}$ mode, i.e., $t_{\mathrm{match}}^{\ell m} = t_{\mathrm{peak}}^{\Omega} + \Delta t_{\mathrm{peak}}^{\ell m}$. The matching interval $\Delta t_{\mathrm{match}}^{\ell m}$ is an adjustable parameter that we fix by reducing the difference against numerical merger-ringdown modes (see Table I).

Finally, the full (inspiral-plunge-merger-ringdown) EOB waveform reads

$$h_{\ell m} = h_{\ell m}^{\mathrm{insp-plunge}}\theta(t_{\mathrm{match}}^{\ell m} - t) + h_{\ell m}^{\mathrm{merger-RD}}\theta(t - t_{\mathrm{match}}^{\ell m}). \tag{32}$$

It was noticed in Ref. [23] that when the lowest QNM frequency is substantially larger than the EOB mode frequency at $t_{\mathrm{match}}^{\ell m}$, the EOB mode frequency will generally grow very rapidly to the QNM frequency immediately after $t_{\mathrm{match}}^{\ell m}$. Such growth in the EOB frequency is much more rapid than what is seen in numerical-relativity frequencies. Moreover, when this happens, the EOB amplitude shows an unphysical "second peak" shape where the ringdown amplitude grows for a while before eventually decaying. The growth of the EOB frequency can be slowed down by including a pseudo QNM [23] that has a frequency close to the EOB mode frequency at $t_{\mathrm{match}}^{\ell m}$ and a decay time comparable but smaller than the decay time of the least damped $n = 0$ QNM. As we shall discuss below, we find it necessary to introduce a pseudo QNM in modeling the EOB (4, 4) and (5, 5) modes. The pseudo QNM should be counted as another adjustable parameter of the EOB waveform (see Table I). The frequency and decay time of this pseudo QNM mode are given in Eq. (41).

We have outlined the procedure to match the inspiral waveform to the merger-ringdown waveform. We would like now to understand what is the *intrinsic* error that this procedure introduces. To answer this question, we build an inspiral-merger-ringdown waveform where the inspiral part coincides with the numerical-relativity waveform, and the merger-ringdown part is built using the EOB procedure. We then extract the intrinsic error by comparing it to the numerical-relativity full waveform. The results for the (2, 2) and (4, 4) modes are shown in Fig. 3. By construction, the two waveforms agree exactly before the matching time $t_{\mathrm{match}}^{\ell m}$, i.e., the time of the peak amplitude. For $h_{22}$, the relative amplitude difference and phase difference during ringdown are about 10% and 0.1 rad. These are reasonable intrinsic errors for the EOB model and are comparable to systematic errors in the best existing analytical models [23,31]. For $h_{44}$, the pseudo QNM reduces the amplitude and phase differences substantially to the level of 50% (when the ringdown amplitude is below 10% of the peak amplitude) and 0.6 rad. Although the differences are not as small as those of $h_{22}$, they are for now acceptable considering the relatively small amplitude of $h_{44}$ compared to $h_{22}$, at least for the mass ratios considered in this paper. So, in the following we shall not attempt to over-calibrate the EOB $h_{44}$ model to obtain smaller differences against the numerical results.

The intrinsic error depends on the procedure to match the inspiral waveform to the merger-ringdown waveform. In particular, it depends on the choice of $t_{\mathrm{match}}^{\ell m}$ and $\Delta t_{\mathrm{match}}^{\ell m}$, as well as the continuity conditions we impose on the points sampled from $t_{\mathrm{match}}^{\ell m} - \Delta t_{\mathrm{match}}^{\ell m}$ to $t_{\mathrm{match}}^{\ell m}$. In Fig. 3, the results are optimized only over $\Delta t_{\mathrm{match}}^{\ell m}$. To find the best matching procedure, in principle, we should optimize over both $t_{\mathrm{match}}^{\ell m}$ and $\Delta t_{\mathrm{match}}^{\ell m}$, and consider options that sample points and impose continuity conditions in different ways. Since the relation between the intrinsic error and all these parameters is not straightforward, we decide to refrain

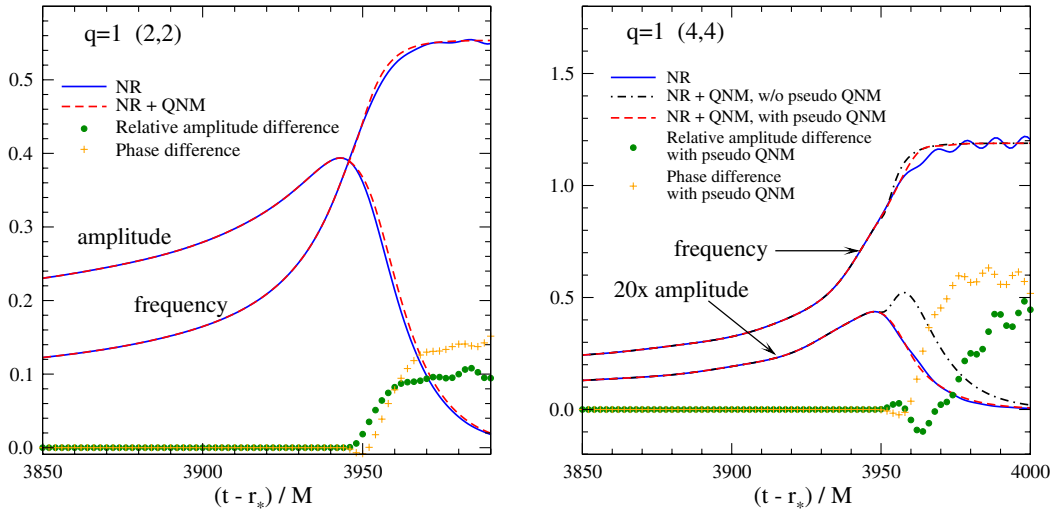


FIG. 3 (color online). Amplitude (in units of $M/\mathcal{R}$) and frequency (in units of $1/M$) comparison between the full "NR" waveform and the "NR + QNM" waveform generated by attaching QNMs to the inspiral-plunge numerical waveform. We show also the relative amplitude and phase differences. In the left panel, we compare $h_{22}$. In the right panel, we compare the numerical $h_{44}$ mode with two "NR + QNM" modes. One of them is generated by attaching the physical QNMs, the other is generated by attaching both the physical QNMs and the pseudo QNM. The former is very different from the numerical-relativity mode and we do not show their amplitude and phase differences. All $h_{44}$ amplitudes have been multiplied by a factor of 20, so that they are more visible. The horizontal axis is the retarded time in the numerical-relativity simulation.

from fine-tuning the ringdown waveform by assigning different matching procedures to different mass ratios or modes. We prefer to use a single, simple prescription that works well for all mass ratios and modes. Thus, we fix $t^{\ell m}_{\rm match}$ to be the peak of the EOB $h_{\ell m}$ waveform and find that this prescription works fairly well.

In summary, there is an intrinsic error introduced by the current procedure to match inspiral to merger-ringdown EOB waveforms. This error cannot be improved by better calibrating the EOB inspiral-plunge dynamics and waveforms. It can be overcome only by improving and/or changing the matching procedure. We leave to the future this important work.

### D. Initial conditions for the EOB dynamics

Before completing this section, we briefly review the way in which initial conditions of the EOB Hamilton Eqs. (10) are implemented.

In Ref. [16], quasispherical initial conditions are given for generic precessing black-hole binaries. We adopt the nonspinning limit of those conditions

$$\frac{\partial \hat{H}^{\rm real}}{\partial r} = 0, \tag{33a}$$

$$\frac{\partial \hat{H}^{\rm real}}{\partial p_{r_*}} = \frac{1}{\nu}\frac{dE}{dt}\frac{(\partial^2 \hat{H}^{\rm real}/\partial r \partial p_\Phi)}{(\partial \hat{H}^{\rm real}/\partial p_\Phi)(\partial^2 \hat{H}^{\rm real}/\partial r^2)}, \tag{33b}$$

$$\frac{\partial \hat{H}^{\rm real}}{\partial p_\Phi} = \Omega_0. \tag{33c}$$

Given the initial orbital frequency $\Omega_0$, we solve the initial $r$, $p_{r_*}$ and $p_\Phi$ from Eqs. (33a)–(33c) and set the initial orbital phase $\Phi = 0$. We always start the orbital evolution at initial orbital frequency $M\Omega_0 \leq 0.0025$, corresponding to an initial radius $r \gtrsim 50M$, such that the binary orbits are sufficiently circularized at the frequency where numerical simulations start.[5]

## III. CALIBRATIONS AND COMPARISONS

In this section we calibrate the EOB model against the numerical simulations, and compare numerical and EOB (2, 2), (2, 1), (3, 3), (4, 4) and (5, 5) modes.

### A. Numerical-relativity simulations of unequal-mass binary black holes

The numerical simulations themselves are described in a separate paper [41]. We extract both the Newman-Penrose modes $\Psi_4^{\ell m}$ and the strain modes $h_{\ell m}$ from the simulations. The strain modes are extracted with the Regge-Wheeler-Zerilli (RWZ) formalism [42,56–58] (see Appendix A of Ref. [23] for details of the numerical implementation used to obtain $h_{\ell m}$). The waveforms are then extrapolated to infinite extraction radius with order $N = 5$ polynomials in the $q = 1$ case, and $N = 3$ polynomials in other cases [43]. In this section, we use the RWZ $h_{\ell m}$ to calibrate the EOB adjustable parameters and to determine the EOB NQC coefficients as functions of the mass ratio. We use the Newman-Penrose mode $\Psi_4^{\ell m}$ only to align numerical and/or EOB waveforms at low frequency where numerical errors of the former are smaller than those of the RWZ $h_{\ell m}$.

We adopt the same waveform alignment procedure used in Refs. [22,23,26]. That is, we align waveforms at low frequency by minimizing the quantity

$$\Xi(\Delta t, \Delta\phi) = \int_{t_1}^{t_2} [\phi_1(t) - \phi_2(t - \Delta t) - \Delta\phi]^2 dt, \tag{34}$$

over a time shift $\Delta t$ and a phase shift $\Delta\phi$, where $\phi_1(t)$ and $\phi_2(t)$ are the phases of the two $\Psi_4^{\ell m}$ waveforms. The range of integration $(t_1, t_2)$ is chosen to be as early as possible to maximize the length of the waveform, but late enough to avoid the contamination from junk radiation present in the numerical initial data. The range of integration should also be large enough to average over numerical noise. Moreover, this range should extend from peak to peak or trough to trough of oscillations (if visible) in the gravitational-wave frequency due to residual eccentricity in the initial data. For different mass ratios, the lengths of numerical simulations and waveforms are different, thus we must also choose different $t_1$ and $t_2$ in Eq. (34). Ref. [59] suggested a minimal length of the integration interval $(t_1, t_2)$ which is satisfied by our choices as listed in Table III.

The numerical uncertainties are estimated by combining convergence errors with extrapolation errors. The convergence estimates also use the matching procedure described above. Specifically, the resolution convergence uncertainty is obtained by matching data from the highest and second highest resolutions over the relevant region from Table III, then taking the relative amplitude and phase difference between them. The same process is repeated for the extrapolation uncertainty, comparing waveforms extrapolated with two orders—the order used in this paper, and the next higher order. Specifically, those orders are $N = 5$ and $N = 6$ for the $q = 1$ case, and $N = 3$ and $N = 4$ for $q = 2, 3, 4, 6$. The absolute values of those uncertainties

TABLE III. The range of integration $(t_1, t_2)$ for waveform alignment and mass ratios $q = 1, 2, 3, 4$ and 6.

| | $q = 1$ | $q = 2$ | $q = 3$ | $q = 4$ | $q = 6$ |
|---|---|---|---|---|---|
| $t_1/M$ | 820 | 770 | 570 | 670 | 870 |
| $t_2/M$ | 2250 | 2255 | 1985 | 1985 | 2310 |

[5]Note that Eq. (33b) is derived in Ref. [16] for $p_r$. At large initial separations, the difference between $p_{r_*}$ and $p_r$ is negligible and we do not distinguish them when setting initial conditions.

are then added to give the final uncertainty estimate. These uncertainties are shown as dotted lines in every figure of this paper where phase and fractional amplitude differences are shown.

### B. Extracting information from numerical-relativity waveforms

As discussed in Secs. II B and II C, we need to extract specific information from the numerical data that we use to determine the NQC coefficients $a_i^{h_{\ell m}}$ and $b_i^{h_{\ell m}}$ in Eq. (22), and the QNM coefficients $A_{\ell mn}$ in Eq. (28).

In Table II we have listed the fitting formulas for the relevant quantities $\Delta t^{\ell m}_{\rm peak}$, $|h^{\rm NR}_{\ell m}(t^{\ell m}_{\rm peak})|$, $d^2|h^{\rm NR}_{\ell m}|/dt^2|_{t^{\ell m}_{\rm peak}}$, $\omega^{\rm NR}_{\ell m}(t^{\ell m}_{\rm peak})$, and $\dot{\omega}^{\rm NR}_{\ell m}(t^{\ell m}_{\rm peak})$. These formulas are least-square fits of numerical-relativity results at mass ratios $q = 1, 2, 3,$ 4 and 6 and numerical results in the test-particle limit $\nu = 0.001$ generated by a time-domain Teukolsky code [60]. The errors of the fitting formulas are worst for the (5, 5) mode and for the quantity $d^2|h^{\rm NR}_{\ell m}|/dt^2|_{t^{\ell m}_{\rm peak}}$. The (5, 5) mode generally has the lowest amplitude among the modes being studied and is therefore mostly contaminated by numerical artifacts. Specifically, we find oscillations in the amplitude of numerical waveforms that are amplified in the process of extrapolating the extraction radii to infinity. Such oscillations modify the position and shape of the peak amplitude and they start to become significant for the (5, 5) mode and the other modes with lower amplitudes. The errors suggest that we can barely model the merger amplitude of the (5, 5) mode for generic mass ratios. Numerical errors prevent us from modeling the merger and ringdown of any other mode with smaller amplitude. The relative error on $d^2|h^{\rm NR}_{\ell m}|/dt^2|_{t^{\ell m}_{\rm peak}}$ may reach a few percent for the (2, 2), (2, 1), (3, 3) and (4, 4) modes. Nevertheless, we find the fitted values accurate enough for constraining the shape of the amplitude peaks. In fact, the error in the EOB merger-ringdown waveform of these modes is dominated by the intrinsic error of the matching procedure discussed in Sec. II C. The error on $\Delta t^{\ell m}_{\rm peak}$ is the error in determining the peak of $|h_{\ell m}|$ in the EOB model. Since the peak of the orbital frequency is used as the reference time of merger in the EOB model, and since it coincides with the peak of the numerical amplitude $h_{22}$ to within $1.8M$ (see Sec. II B), the $0.5M$ error in fitting $\Delta t^{33}_{\rm peak}$ and $\Delta t^{21}_{\rm peak}$ is sufficiently small. The relative errors in fitting all other quantities are within 1% and we expect these fitting formulas to work with such accuracy for any mass ratio $q \leq 6$.

It is interesting to observe that the reason why the shape and characteristics of the numerical amplitude peaks can be easily reproduced by polynomials in $\nu$ (see Table II) rests on the fact that when the modes for different $\nu$ are aligned at the peak and rescaled by $\nu$, their peaks differ by less than 7% and the width at half peak by less than 18%. This is illustrated in Fig. 4, and was initially pointed out in Ref. [52].

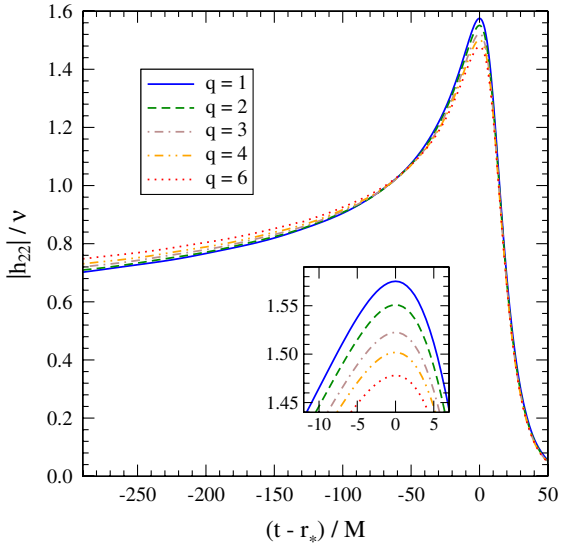


FIG. 4 (color online). We show the amplitude of the numerical-relativity $h_{22}$ for mass ratios $q = 1, 2, 3, 4, 6$. We have time shifted the modes so that their peaks are aligned. We have also rescaled them by $\nu$. The horizontal axis is the retarded time in the numerical-relativity simulation. The inset shows an enlargement of the merger region.

### C. Calibrating the EOB adjustable parameters

We carry out the calibration of the adjustable parameters as follows. First, we fix the EOB-dynamics parameters by minimizing the phase difference between the numerical and EOB (2, 2) modes during the inspiral. Second, we evolve the EOB dynamics with the calibrated parameters and fix the EOB-waveform parameters by minimizing the difference between the numerical and EOB full waveforms of all relevant modes. Moreover, the adjustable parameters might be functions of the mass ratio $\nu$. So, we first calibrate them for individual mass ratios then fit the calibrated values with quadratic functions of $\nu$. We find that many parameters depend weakly on $\nu$ and can be set as constants.

Figure 5 summarizes the calibration result of the inspiral dynamics and our choice of the $a_5(\nu)$ and $a_6(\nu)$ values. We calibrate the EOB model to five numerical $h_{22}$ waveforms of mass ratios $q = 1, 2, 3, 4$ and 6. For each mass ratio, we show a contour in the $a_5(\nu)/\nu - a_6(\nu)/\nu$ parameter space in which the numerical and EOB $h_{22}$ waveforms agree in phase to within 0.2 rad at merger, that is, at the peak of the (2, 2) mode. As observed in Ref. [31] (and also evident from Fig. 5), there is strong degeneracy between $a_5(\nu)$ and $a_6(\nu)$. Furthermore, there are many ways to choose $a_5(\nu)$ and $a_6(\nu)$ so that the numerical and EOB $h_{22}$ waveforms agree for $q = 1, 2, 3, 4$ and 6. For instance, we could choose a point near $a_5(\nu)/\nu = -10$ and $a_6(\nu)/\nu = 126$ where the contours of different mass ratios approximately cross. However, we find that those values do not satisfy the constraint imposed by the self-force result of the ISCO

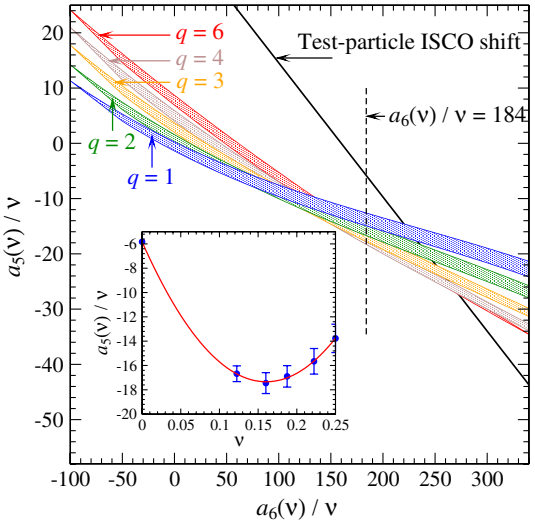


FIG. 5 (color online). We calibrate adjustable parameters of the EOB dynamics. For mass ratios $q = 1$, 2, 3, 4 and 6, the shaded regions correspond to $(a_5, a_6)$ values for which the EOB and numerical-relativity $h_{22}$ agree within 0.2 rad at merger, i.e., at the peak of the numerical $h_{22}$. In the inserted subplot, for $a_6(\nu)/\nu = 184$, we show $a_5(\nu)/\nu$ values constrained by the shaded regions and by the test-particle ISCO-shift result [61], and also the quadratic fit (red curve) given by Eq. (36a).

shift of Ref. [61]. More importantly, even if we chose not to impose the ISCO shift prediction, the EOB model obtained by choosing $a_5(\nu)/\nu$ and $a_6(\nu)/\nu$ around that crossing region will not be very satisfactory, because the point will not lie in the middle of the contours for each mass ratio.

By contrast, we follow a more satisfactory route. We decide to model $a_5(\nu)/\nu$ and $a_6(\nu)/\nu$ as generic quadratic functions of $\nu$, i.e., $a_5(\nu)/\nu = \sum_{i=0}^{2} a_5^{(i)} \nu^i$ and $a_6(\nu)/\nu = \sum_{i=0}^{2} a_6^{(i)} \nu^i$. In the test-particle limit $\nu \to 0$, we impose the constraint on $a_5^{(0)}$ and $a_6^{(0)}$ that the conservative EOB dynamics incorporates the exact ISCO-frequency shift of the self-force calculation [61], that is [47],

$$M\Omega_{\rm ISCO} = 6^{-3/2}[1 + 1.2513\nu + \mathcal{O}(\nu^2)]. \quad (35)$$

The remaining five coefficients of $a_5^{(i)}$ and $a_6^{(i)}$ are determined by minimizing the distances of the $a_5(\nu)/\nu - a_6(\nu)\nu$ points to the center of the contours in Fig. 5 (i.e., the points at equal distance from the top and bottom boundaries of the contours) for mass ratios $q = 1$, 2, 3, 4 and 6. This procedure is not unique; we optimize $a_5^{(i)}$ and $a_6^{(i)}$ over a relatively coarse grid and find reasonable results setting $a_6(\nu)/\nu$ as a constant and

$$a_5(\nu) = (-5.828 - 143.5\nu + 447\nu^2)\nu, \quad (36a)$$

$$a_6(\nu) = 184\nu. \quad (36b)$$

For this constant choice of $a_6(\nu)/\nu$, we show in a subplot of Fig. 5 the $a_5(\nu)/\nu$ values constrained by the contours, as well as the quadratic fit of them. The error bars correspond to the width of the contours. More constraints imposed by new numerical waveforms may further lift the degeneracy between $a_5(\nu)$ and $a_6(\nu)$. We shall show in the next section that this model calibrated to the five numerical waveforms, even though not carefully optimized with a fine global grid, is good enough for detection with Advanced LIGO, and fair for parameter estimation purposes.

Although $a_5(\nu)/\nu$ and $a_6(\nu)/\nu$ cannot both be constants in this calibrated model, we shall emphasize that it does not imply that the physical 4PN and 5PN coefficients shall depend on $\nu$ beyond the linear order. The optimal choice of $a_5(\nu)$ and $a_6(\nu)$ depends on other elements of the dynamics, for instance, the Padé expression of $A(r)$ or $D(r)$, or the way we factorize or resum $h^{\rm F}_{\ell m}$ in the inspiral waveforms that enter the energy flux, etc. Therefore, it is possible that when a different EOB model is calibrated to the same set of numerical waveforms subject to the constraint imposed by the self-force result, the optimal choice of $a_5(\nu)/\nu$ and $a_6(\nu)/\nu$ are constants. It might be the case that a minor change in the dynamics of the EOB model being calibrated in this paper could bring all contours and the self-force constraint to cross at exactly the same point.

Having calibrated the adjustable parameters of the EOB dynamics, we calibrate the adjustable parameters of the EOB waveform listed in Table I, notably the width of the comb $\Delta t^{\ell m}_{\rm match}$, a few higher-order PN terms in $\rho_{\ell m}$ and $\delta_{\ell m}$ (see Appendix B), and a pseudo QNM. For technical reasons we do not include the adjustable parameters $\rho_{21}$, $\rho_{33}$, $\rho_{44}$, and $\rho_{55}$ in the energy flux (12), but only in the EOB modes (13). The energy flux being used in the dynamical evolution is therefore slightly different from the energy flux defined in Eq. (12). For the mass ratios and length of waveforms being considered in this paper, the fractional difference in the energy flux grows from $\sim 10^{-4}$ during low frequency to $\sim 10^{-2}$ at merger. Such a difference in the dynamics generates a phase difference at merger that increases from 0.02 rad to 0.35 rad with mass ratio increasing from $q = 1$ to $q = 6$. In principle, to have an energy flux in the dynamics that is exactly consistent with the definition in Eq. (12), we need to calibrate those adjustable parameters in $\rho_{\ell m}$ as EOB-dynamics parameters, together with $a_5$ and $a_6$. Calibrating a large number of EOB-dynamics parameters has two consequences: the calibration becomes computationally expensive and all parameters become highly degenerate. Because of these technical difficulties and the relatively small fractional difference in the flux, we choose not to include the adjustable parameters in $\rho_{\ell m}$ in the energy flux.

We determine the width of the comb $\Delta t^{\ell m}_{\rm match}$ by requiring the best agreement between EOB and numerical $h_{\ell m}$ around merger and ringdown. We find that $\Delta t^{\ell m}_{\rm match}$ depends

moderately on the mass ratio, and we can assume $\Delta t^{\ell m}_{\rm match}$ to be a constant. Specifically, we obtain

$$\Delta t^{22}_{\rm match} = 5M, \tag{37a}$$
$$\Delta t^{33}_{\rm match} = 12M, \qquad \Delta t^{44}_{\rm match} = 9M, \tag{37b}$$
$$\Delta t^{21}_{\rm match} = 8M, \qquad \Delta t^{55}_{\rm match} = 8M. \tag{37c}$$

Calibrating the amplitude and phase of the EOB waveform for the higher-order modes we find

$$\rho^{(6)}_{21} = -5, \qquad \rho^{(6)}_{33} = -20, \tag{38a}$$
$$\rho^{(6)}_{44} = -15, \qquad \rho^{(6)}_{55} = 4, \tag{38b}$$

and

$$\delta^{(7)}_{21} = 30, \qquad \delta^{(7)}_{33} = -10, \tag{39a}$$
$$\delta^{(5)}_{44} = -70, \qquad \delta^{(5)}_{55} = 40. \tag{39b}$$

As explained in Sec. II B, since the iterative procedure that determines the NQC coefficients $a^{h_{22}}_i$ usually takes four to five steps to converge, we give fitting formulas of $a^{h_{22}}_i$ as quadratic functions of the mass ratio to save computational cost:

$$a^{h_{22}}_1(\nu) = -4.559 + 18.76\nu - 24.23\nu^2, \tag{40a}$$
$$a^{h_{22}}_2(\nu) = 37.68 - 201.5\nu + 324.6\nu^2, \tag{40b}$$
$$a^{h_{22}}_3(\nu) = -39.6 + 228.9\nu - 387.2\nu^2. \tag{40c}$$

Finally, as discussed in Sec. II C, to improve the agreement of the (4, 4) and (5, 5) modes around merger, we introduce pseudo QNMs having

$$M\omega^{\rm pQNM}_{44} = 0.72, \qquad M/\tau^{\rm pQNM}_{44} = 0.28, \tag{41a}$$
$$M\omega^{\rm pQNM}_{55} = 0.9, \qquad M/\tau^{\rm pQNM}_{55} = 0.28, \tag{41b}$$

for all mass ratios considered in this paper. The frequency of these pseudo QNMs are about the frequency of the inspiral-plunge waveforms at the matching time $t^{\ell m}_{\rm match}$ and the decay time of these modes are about the same as that of the first overtone of the physical QNMs.

### D. Comparing numerical and EOB (2, 2) mode

In Figs. 6 and 7 we compare the numerical-relativity and EOB (2, 2) modes for mass ratios $q = 1, 2, 3, 4$ and 6. We find that throughout the evolution the phase difference is below $\sim$0.1 rad. During the inspiral, the relative amplitude difference is within 2%, while during merger and ringdown it increases to within 12%. The numerical errors are also shown in the figures with dotted lines. We observe that during the inspiral the phase and amplitude differences can be a factor of a few larger than the numerical-relativity error, but during the merger and ringdown they can be comparable or even smaller. As we shall see in Sec. IV, the mismatch between the numerical and EOB modes

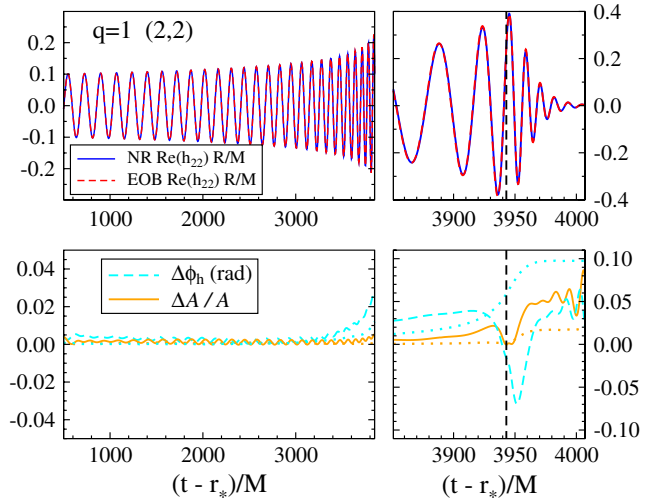


FIG. 6 (color online). For the equal-mass case, we compare the numerical-relativity and calibrated EOB (2, 2) mode. The top panels show the real part of numerical and EOB $h_{22}$, the bottom panels show amplitude and phase differences between them. The horizontal axis is the retarded time in the numerical-relativity simulation. The left panels show retarded times $t - r_* = 0$ to $3850M$, and the right panels show retarded times $t - r_* = 3850M$ to $t - r_* = 4070M$ on a different vertical scale. The dotted curves are the numerical-relativity errors.

are consistently very small for detection purposes for Advanced LIGO, and the EOB modes are reasonably accurate for parameter-estimation purposes.

### E. Comparing numerical and EOB $(l, m) \neq (2, 2)$ modes

In Figs. 8–10, we compare the numerical and EOB subdominant modes $h_{33}$, $h_{21}$ and $h_{44}$ for the cases $q = 1$, 3, 6. [For mass ratios $q = 2, 4$ the plots look similar, so we do not show them.] During the inspiral, the numerical and EOB subdominant modes agree very well, similar to the agreement we found for the $h_{22}$. This happens because the numerical frequencies $\omega_{\ell m}$ are well modeled by a simple multiple of the orbital frequency $m\Omega$. During merger and ringdown, the agreement is very good for the $h_{33}$ and $h_{21}$ modes, i.e., comparable to the agreement of the $h_{22}$ mode. Analogous performances hold for the other cases $q = 2$ and $q = 4$. The numerical and EOB $h_{44}$ mode, however, show larger differences during ringdown. For instance, the phase difference increases to $\sim$0.6 rad. There are two reasons for this less satisfactory result: (i) the larger errors in the numerical mode (4, 4) and (ii) the EOB QNM matching procedure that generates the ringdown part. Issue (i) spoils the numerical predictions of the fitting formulas for the (4, 4) mode (see Table II) which are essential to model the merger. Issue (ii) prevents modeling the ringdown phase of the $h_{44}$ with high accuracy (see Fig. 3 and discussions therein). Nevertheless, since as seen in Fig. 1, the $h_{44}$ amplitude is a few percent of the

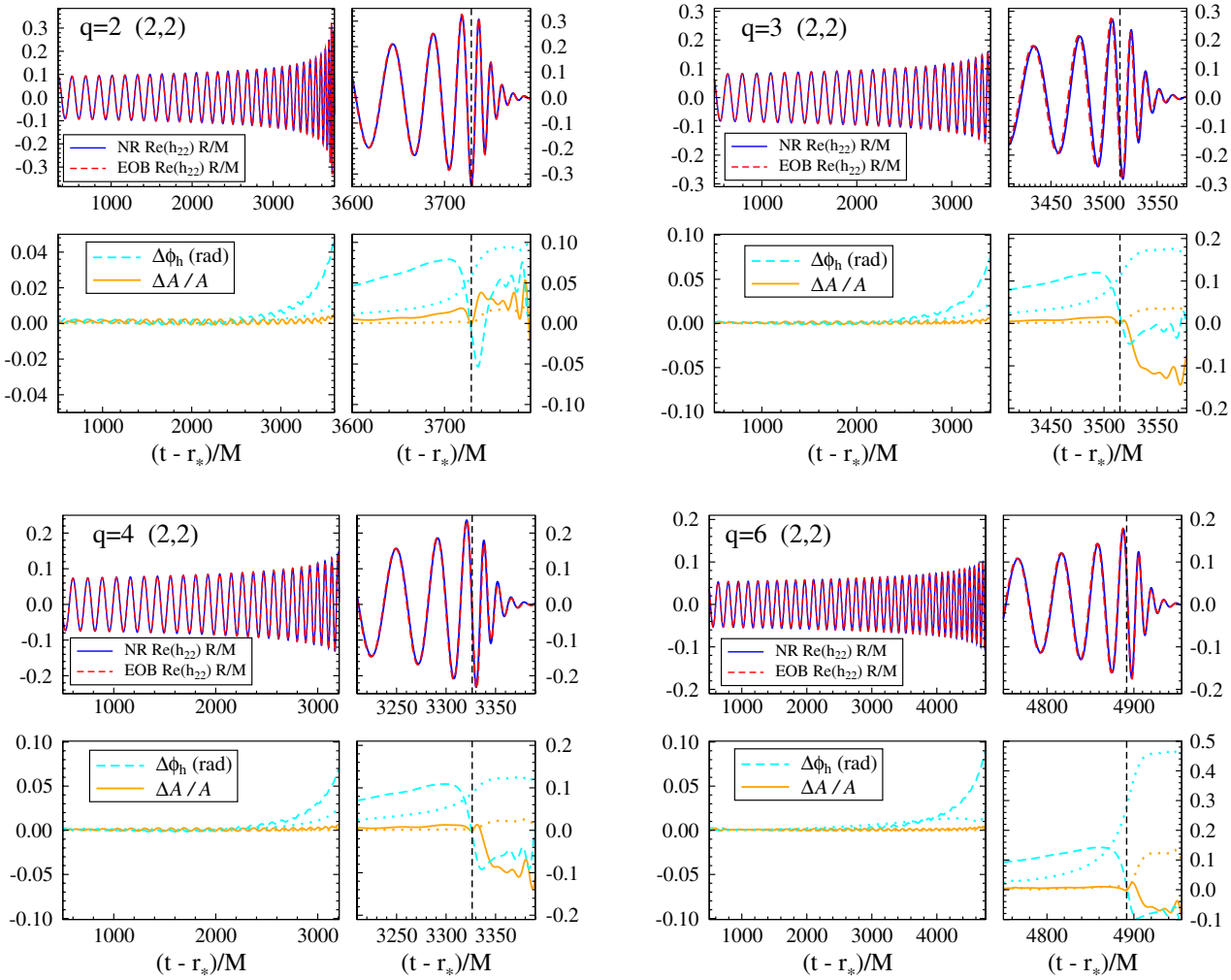


FIG. 7 (color online). Comparison between the (2, 2) modes of the numerical-relativity simulation and the calibrated EOB model for mass ratios $q = 2, 3, 4, 6$. In each subplot, the top panels show the real part of the $h_{22}$ mode and the bottom panels show the phase and amplitude differences between numerical and EOB waveform. The dotted curves are the numerical-relativity errors.

$h_{22}$ amplitude, the absolute error in $h_{44}$ is generally smaller than the error with which we currently model the $h_{22}$ EOB mode. Therefore, the large difference between the numerical and EOB $h_{44}$ is not the dominant source of systematic error in the gravitational polarizations. Since the $h_{55}$ mode comparison is very similar to that of the (4, 4) mode, except for an even larger phase difference of $\sim$1 rad during ringdown, we do not show it for brevity. Modeling the $h_{55}$ mode is difficult due to the same two issues discussed above, while on a more severe level. Nevertheless, we find in Sec. IV that there is substantial benefit in including this mode in the full polarization waveforms even though its modeling is not fully satisfactory.

We point out that the special treatment of the (2, 1) and (4, 4) modes in Eq. (17), namely, the replacement of $v_\Phi^{(\ell+\epsilon)}$ with $v_\Phi^{(\ell+\epsilon-2)}/r_\Omega$ for these modes, was necessary to improve the agreement of these modes with the numerical waveforms. Equation (17) was suggested by similar studies in the test-particle limit [60]. The reason is the following: as shown in Fig. 1 the amplitudes of the numerical (2, 1) and (4, 4) modes reach a peak quite after the peak of the (2, 2) mode, i.e., they have large, positive $\Delta t^{\ell m}_{\rm peak}$ values. If we want to impose the condition 1 listed in Sec. II B, the peak of the EOB mode should be moved to $t^{\Omega}_{\rm peak} + \Delta t^{\ell m}_{\rm peak}$. However, the EOB Newtonian amplitude is proportional to a power of the orbital frequency and the latter decreases to zero at the EOB horizon, thus the EOB amplitude drops to an extremely small value at $t^{\Omega}_{\rm peak} + \Delta t^{\ell m}_{\rm peak}$. By contrast, replacing $v_\Phi^2 = (r_\Omega \Omega)^2$ with $1/r_\Omega$, we slow down the decay of these modes after $t^{\Omega}_{\rm peak}$, and we can successfully move the peak of the mode to $t^{\Omega}_{\rm peak} + \Delta t^{\ell m}_{\rm peak}$. Note that $v_\Phi^2$ and $1/r_\Omega$ are exactly the same in the adiabatic Keplerian limit. This replacement introduces higher-order nonadiabatic non-Keplerian corrections that have negligible effects on the inspiral waveform and the energy flux. During plunge and merger, perturbative treatments break down and there is no *a priori* justification in describing the

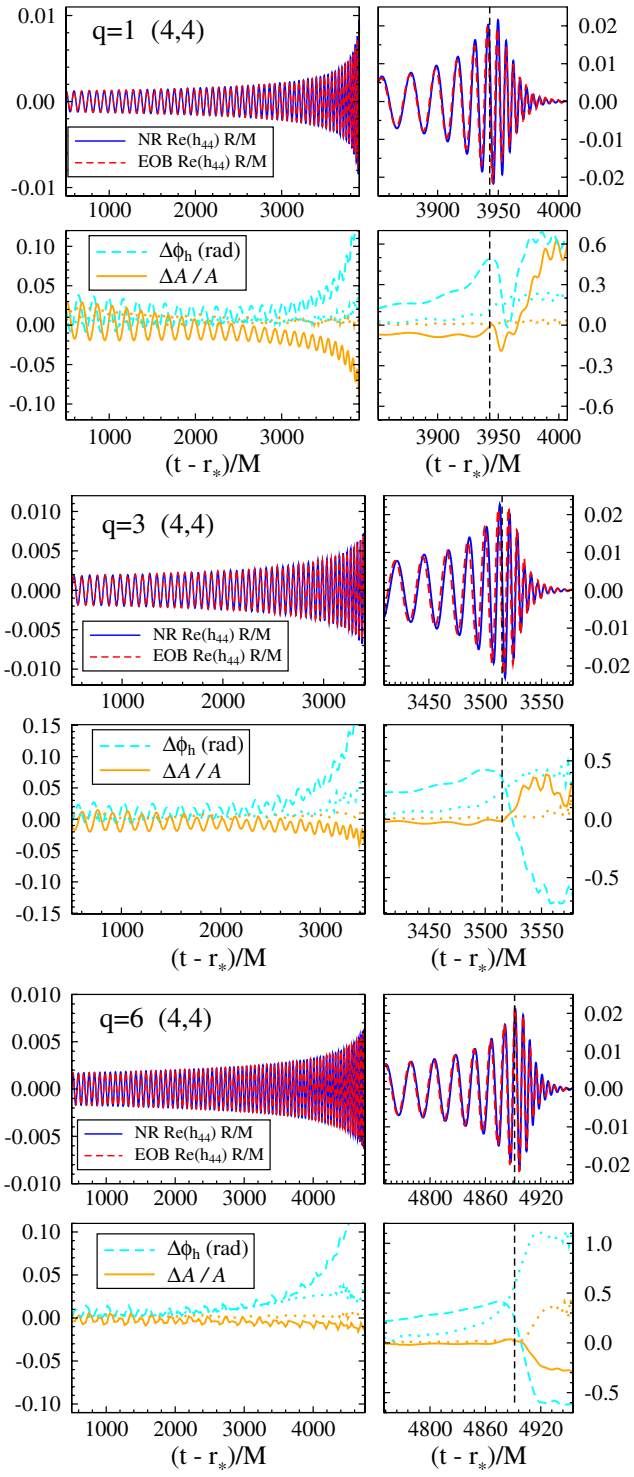


FIG. 8 (color online). Comparison of the (4, 4) mode for mass ratios $q = 1, 3, 6$ between numerical and calibrated EOB model. Plotted data as in Fig. 7.

mode amplitude with a power of either $v_\Phi$ or $1/r_\Omega$. Equation (17) is adopted since combined with the NQC corrections, it is capable of reproducing the numerical-relativity waveforms during merger. To make minimal adjustments to the Newtonian term of Eq. (16), we

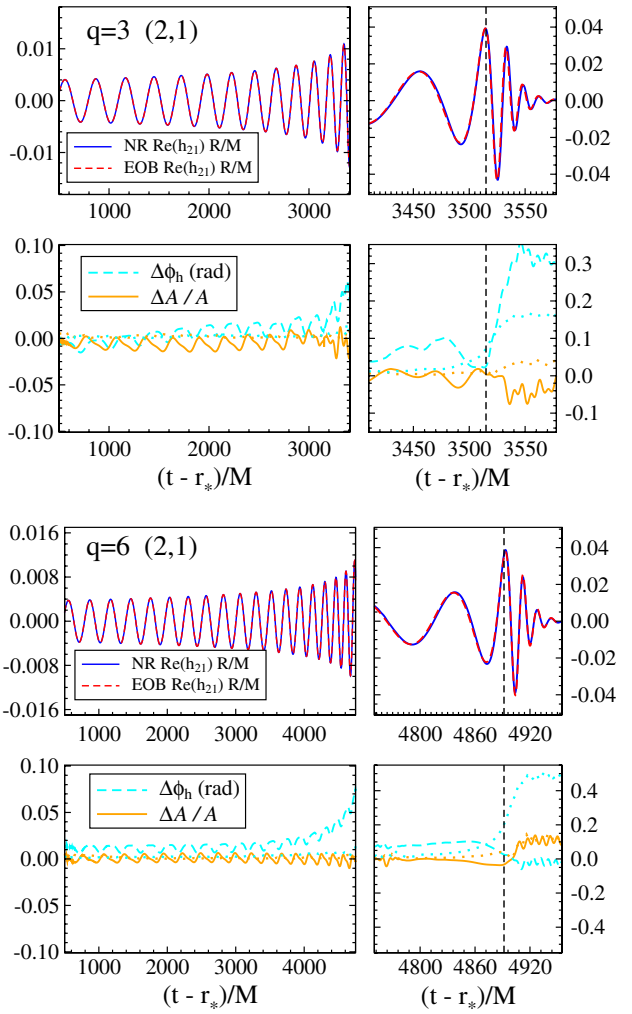


FIG. 9 (color online). Comparison of the (2, 1) mode for mass ratios $q = 3$ (top panel) and $q = 6$ (bottom panel) between numerical and calibrated EOB model. Plotted data as in Fig. 7.

introduce this replacement only when needed, i.e. to the (2, 1) and (4, 4) modes.

## IV. EFFECTUALNESS AND MEASUREMENT ACCURACY OF EOB WAVEFORMS

In this section, we examine the effectualness and measurement accuracy of the EOB waveforms in matching the numerical-relativity waveforms.

These investigations utilize the noise-weighted inner product between two waveforms $h_i$, $i = 1, 2$:

$$\langle h_1, h_2 \rangle \equiv 4\Re \int_0^\infty \frac{\tilde{h}_1(f)\tilde{h}_2^*(f)}{S_h(f)} df, \tag{42}$$

where $\tilde{h}_i(f)$ are the Fourier transforms of $h_i(t)$, and $S_h(f)$ is the spectral density of noise in the detector. We choose one of the Advanced LIGO noise curves, named ZERO_DET_HIGH_P in Ref. [62].

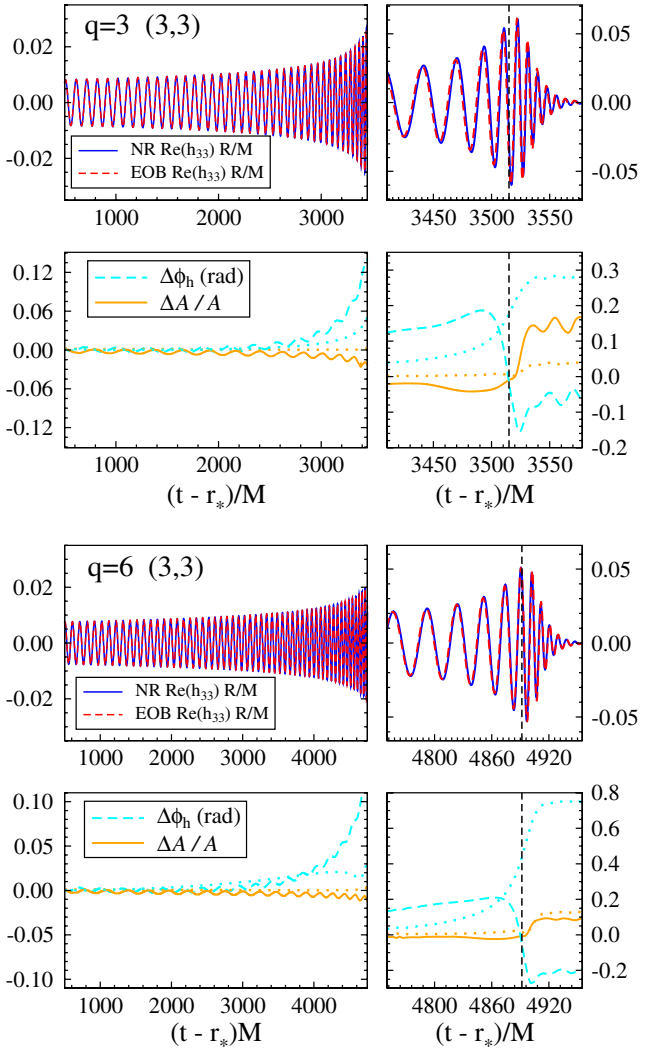


FIG. 10 (color online). Comparison of the (3, 3) mode for mass ratios $q = 3$ (top panel) and $q = 6$ (bottom panel) between numerical and calibrated EOB model. Plotted data as in Fig. 7.

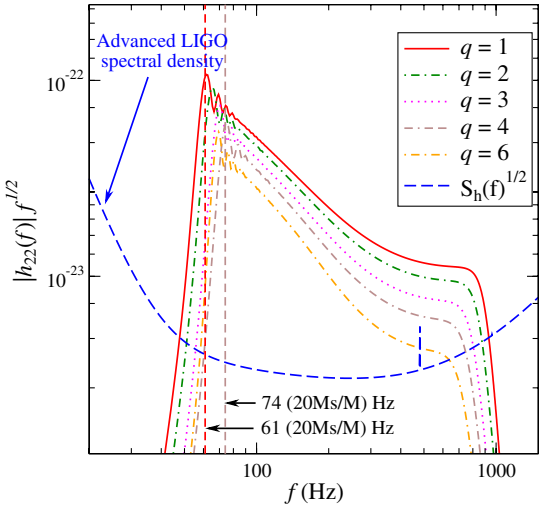


FIG. 11 (color online). Amplitude of the Fourier transform of the (2, 2) mode of the numerical-relativity waveforms, scaled to a total mass $M = 20M_\odot$. We also plot the noise spectral density of the Advanced LIGO detector. The two vertical lines mark the initial gravitational-wave frequency for the numerical waveforms with $q = 1$ and $q = 4$ (lowest and highest start frequency of all considered waveforms).

Figure 11 shows the noise curve, and the amplitudes of the Fourier transforms of the numerical relativity waveforms. For the binary's total masses considered, the NR waveforms start in band; to reduce artifacts from this, we taper the NR waveforms using the Planck-taper window function [63]. The width of the window function is set to the length of numerical-relativity waveforms, which is about $0.5(M/20M_\odot)$ seconds. The window function smoothly rises from 0 to 1 in the first 0.0625 seconds and falls from 1 to 0 in the last 0.0125 seconds. Furthermore, whenever we compute quantities involving both an NR waveform and an EOB waveform (e.g., an overlap; see below), we restrict integration of the EOB waveform to the frequency for which numerical data is available.

Figure 11 indicates the initial gravitational-wave frequency of the $q = 1$ and $q = 4$ simulations. The simulation with $q = 1$ has the lowest initial gravitational-wave frequency, while the one with $q = 4$ has the largest initial gravitational-wave frequency. The numerical-relativity waveforms for mass ratios $q = 1, 2, 3, 4, 6$ have 32, 31, 31, 31, and 43 gravitational-wave cycles, respectively, from the initial frequency to the peak of the (2, 2) mode. Using the EOB model of this paper we estimate that for a total mass of $20M_\odot$ and mass ratios $q = 1, 2, 3, 4, 6$, there are 582, 656, 779, 914, 1184 gravitational-wave cycles between 10 Hz and the start of the numerical-relativity simulations. These missing cycles, which decrease as the total mass of the binary increases, are not accounted for when computing mismatches.

### A. Subdominant modes

To investigate the importance of subdominant modes $(l, m)$ different from (2, 2), we consider the gravitational waveform emitted from the binary into a given sky direction $(\theta, \phi)$ (as measured relative to the orbital plane of the binary and note that $\phi$ is degenerate with the initial phase), given as

$$h_+(\theta, \phi; t) - ih_\times(\theta, \phi; t) = \sum_{\ell,m} {}_{-2}Y_{\ell m}(\theta, \phi) h_{\ell m}(t). \quad (43)$$

Here ${}_{-2}Y_{\ell m}(\theta, \phi)$ is the $-2$ spin-weighted spherical harmonic, and the summation on $\ell$ and $m$ is over the available NR or EOB modes.[6] In the remainder of this

[6]In the numerical simulations, seven modes (14 modes if we count $m < 0$) are extracted: $(\ell, m) = (2, 2), (2, 1), (3, 3), (3, 2), (4, 4), (5, 5), (6, 6)$. In the EOB model, five modes (10 modes if we count $m < 0$) are calibrated in Secs. III D and III E: $(\ell, m) = (2, 2), (2, 1), (3, 3), (4, 4), (5, 5)$.

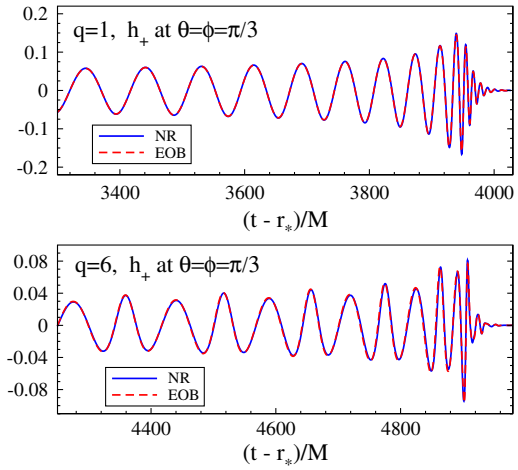


FIG. 12 (color online). The polarization waveform $h_+(\theta, \phi; t)$ as emitted into sky direction $\theta = \phi = \pi/3$. *Top panel*: mass ratio $q = 1$; *bottom panel*: mass ratio $q = 6$. The solid blue curve represents the numerical data, the red dashed curve the EOB model, and only late inspiral, merger and ringdown are shown.

section, we always choose $\theta = \pi/3$ and $\phi = \pi/3$, and assume a relative binary-detector configuration such that the detector is only sensitive to $h_+$ (i.e., an antenna pattern $F_+ = 1$, $F_\times = 0$). A comprehensive study of arbitrary gravitational polarizations for all sky directions $\theta$, $\phi$ is left to future work.

Figure 12 shows the resulting waveforms $h_+(\pi/3, \pi/3; t)$ for the mass-ratios $q = 1$ and $q = 6$. This figure clearly shows that for $q = 6$, subdominant modes are more important, and one immediately expects that disregarding subdominant modes will have a larger effect for the $q = 6$ case. Let us now quantify these expectations.

### B. Effectualness

The effectualness can be described by the mismatch ($\mathcal{M}$) between two time-domain waveforms $h_1$ and $h_2(t_0, \phi_0, \boldsymbol{\lambda})$. Here, we consider all waveforms to be the $+$ polarization evaluated in the direction $\theta = \phi = \pi/3$ [see Eq. (43)]. We take $h_1$ to be the numerical-relativity waveform at one of the simulated mass ratios for some given total mass $M$. The second waveform $h_2$ is taken to be our calibrated EOB model, where we have explicitly displayed the dependence of this waveform on some reference time $t_0$ and reference phase $\phi_0$, as well as the masses $m_1$ and $m_2$ represented in the vector $\boldsymbol{\lambda}$ of the parameters of the binary.

The mismatch is given explicitly by [21]

$$\mathcal{M} \equiv 1 - \max \frac{\langle h_1, h_2(t_0, \phi_0, \boldsymbol{\lambda})\rangle}{\|h_1\|\|h_2(t_0, \phi_0, \boldsymbol{\lambda})\|} \tag{44}$$

where

$$\|h_i\| = \langle h_i, h_i\rangle^{1/2} \tag{45}$$

denotes the norm induced by Eq. (42). When searching for the signal waveform $h_1$ with the template $h_2(t_0, \phi_0, \boldsymbol{\lambda})$, the horizon distance is reduced by a factor $\mathcal{M}$ relative to searching with the perfect template $h_1$, and the reduction in event rate is given by $1 - (1 - \mathcal{M})^3 \approx 3\mathcal{M}$. Ideally, the maximization in Eq. (44) is over $\{t_0, \phi_0, \boldsymbol{\lambda}\}$; however, sometimes we choose to neglect maximization over $\boldsymbol{\lambda}$, as detailed below.

Figure 13 presents several mismatch calculations for the equal-mass case. The solid lines compare the numerical-relativity data to the leading (2, 2) mode of our EOB model. For these two curves, maximization of $\mathcal{M}$ is performed over $\{t_0, \phi_0, \boldsymbol{\lambda}\}$. If the numerical waveform is represented only by its (2, 2) mode, then the mismatches are very small, reaching $\sim 10^{-4}$. However, if the 7-mode numerical waveform is used with all modes shown in Fig. 1, then the mismatch increases by about an order of magnitude, showing that subdominant modes are noticeable even for the $q = 1$ case.

The two dashed curves in Fig. 13 use the calibrated EOB model with all five calibrated modes included. For these two curves, we maximize the mismatch only over $\{t_0, \phi_0\}$, for technical convenience and to save computational cost. Therefore the obtained mismatches are only upper bounds. We see that the 5-mode EOB model agrees significantly better with the 7-mode NR waveform than an EOB model utilizing only the (2, 2) mode. The line "5-mode NR vs 5-mode EOB" compares NR with EOB

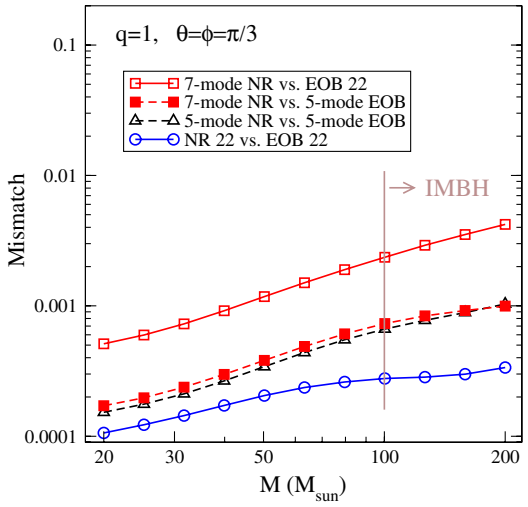


FIG. 13 (color online). The mismatch versus binary total mass for $q = 1$ using Advanced LIGO noise curve. Mismatches with the (2, 2) mode of the EOB waveform are optimized over $\{t_0, \phi_0, \boldsymbol{\lambda}\}$ whereas mismatches with the 5-mode EOB model are optimized over $\{t_0, \phi_0\}$ only and represent an upper bound. The vertical line represents the maximum total mass for stellar-mass black-hole binaries, assuming a maximum black-hole mass of $50M_\odot$. The range of total masses on the right of the vertical line refer to intermediate-mass black-hole binaries.

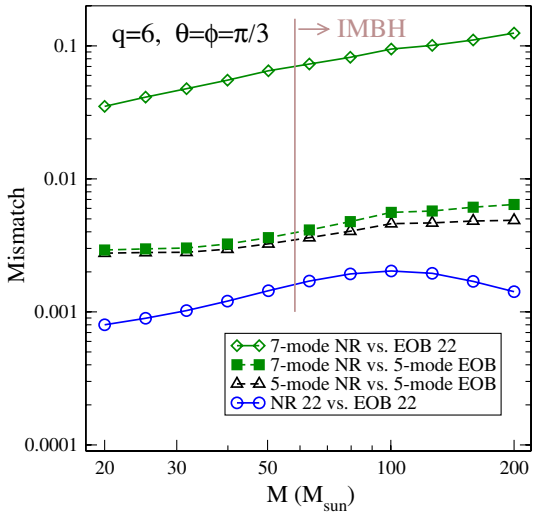


FIG. 14 (color online). Mismatch calculation for mass ratio $q = 6$. All details as in Fig. 13. This figure and Fig. 13 use the same vertical axis to ease comparisons between them.

when both waveforms contain only those five modes for which we calibrate the EOB model.

In Figs. 13–15 we have marked total mass $100M_\odot$ and $58.3M_\odot$ for $q = 1$ and $q = 6$, respectively, the largest masses for *stellar-mass* binary black holes, assuming that the maximum black-hole mass is $\sim 50M_\odot$.[7] More massive black holes are referred to as *intermediate-mass* black holes. Their existence and gravitational-wave event rates are more uncertain [67,68].

Figure 14 presents the analogous calculations to Fig. 13 for mass ratio $q = 6$. The mismatches are generally larger, owing to the more complex waveform of a $q = 6$ binary. The numerical (2, 2) mode can still be fit by a (2, 2) EOB waveform to $\mathcal{M} \sim 10^{-3}$. However, trying to represent the 7-mode NR waveform with only the EOB (2, 2) mode results in mismatches $\sim 7\%$ for total mass $M \sim 58.3M_\odot$ and above 10% for total mass $M \sim 200M_\odot$. Thus, it is extremely important to accurately model higher-order modes when the merger and ringdown waveforms are in band and binary systems contain intermediate-mass black holes with $\gtrsim 50M_\odot$. So far, higher-order modes have been largely ignored in the analysis of real detector data (see for instance Ref. [33]), and by including a few dominant ones, the event rate or the horizon distance can be substantially increased, especially for high total masses.

Inclusion of the higher-order modes reduces the mismatches by a factor of 10 to $\sim 5 \times 10^{-3}$ at low masses and $\sim 0.01$ at high masses, caused mainly by the error in modeling the ringdown waveforms of the higher-order modes. The (3, 2) and (6, 6) modes that are not modeled or included in the EOB polarizations are not responsible for the comparatively large mismatch. To verify this, we show in these figures also the mismatches between the 5-mode EOB polarizations and 5-mode numerical polarizations that contain the same modes as the EOB ones.[8] More diagnostic tests show that the error in modeling the (5, 5) mode is responsible for about half the increase in $\mathcal{M}$, because the phase error of the (5, 5) mode accumulates faster due to its higher frequency, and because it is larger than the phase error of other modes.

As in Fig. 13, mismatches with the 5-mode EOB model are not optimized over $\boldsymbol{\lambda}$ and represent therefore merely upper limits.

We emphasize again that these mismatches measure the difference between numerical-relativity and EOB waveforms only over the frequency band where numerical-relativity simulations are available (see Fig. 11). For large masses, say $M = 100M_\odot$, the initial frequency of the numerical-relativity (2, 2) mode for $q = 6$ is 15 Hz, and the missing part between 10 Hz and 15 Hz would likely modify the mismatches only marginally because of the steeply rising seismic-noise wall toward low frequency. However, for $M = 20M_\odot$ and $q = 6$, the initial frequency of the numerical-relativity (2, 2) mode is 70 Hz which is in the frequency band of the detector. In this case we miss the portion of the numerical-relativity waveform between 10 Hz and 70 Hz. The best way, though time-consuming, to address this gap problem is to produce longer numerical-relativity waveforms, or to conduct tests within the analytical models to assess their reliability below a certain frequency [21,59,69–72]. With the caveat of this frequency gap, we conclude that our calibrated EOB model is sufficient for detection purposes.

### C. Measurement accuracy

We are now interested in the question of whether the EOB polarizations are accurate enough to be used in data analysis for measurement purposes. We adopt as accuracy requirement for measurement the one proposed by [73,74]

$$\|\delta h\| < \epsilon, \tag{46}$$

where $\delta h = h^{\rm EOB}(t) - h^{\rm NR}(t)$ is the error in modeling the numerical waveforms, and $\epsilon < 1$ incorporates a safety factor [71] or the effect of a detector network [59]. The left hand side in Eq. (46) increases proportionally with the signal-to-noise ratio (SNR) $\|h^{\rm NR}\|$ and we calculate the upper bound of the $\mathrm{SNR}^{\rm eff} \equiv \mathrm{SNR}/\epsilon$ that satisfies Eq. (46). For any SNR below this upper bound, the EOB waveforms or polarizations are accurate enough for measurement purposes, i.e., accurate enough not to generate any systematic bias that is larger than statistical errors

[7] As of today, the heaviest mass of a single black-hole source is $23$–$34M_\odot$ [64,65], but considering the possibility of lower metallicity we adopt as maximum mass of a black hole $\sim 50M_\odot$ [66].

[8] Sometime the mismatches increase by $\sim 0.1\%$ after we remove the (3, 2) and (6, 6) modes from the numerical-relativity polarizations. This happens because the numerical precision of our code in optimizing over the initial phase is $\sim 0.1\%$.

in estimating the physical binary parameters. The upper bound $\mathrm{SNR}^{\mathrm{eff}}$ is therefore a very strict accuracy requirement. Unlike the well-known fact that good phase agreement is critical for obtaining good effectualness, to get high (upper bounds on) $\mathrm{SNR}^{\mathrm{eff}}$, both the amplitude and the phase of the templates must agree very well with those of the exact waveforms.

In Fig. 15, for mass ratios $q = 1$ and $q = 6$, we show the upper bound of the $\mathrm{SNR}^{\mathrm{eff}}$ as a function of the total mass. These $\mathrm{SNR}^{\mathrm{eff}}$ are calculated for a single Advanced LIGO detector. In the $q = 1$ case, the 5-mode EOB polarizations match the 7-mode numerical polarizations accurately enough for any $\mathrm{SNR}^{\mathrm{eff}} < 24$ when the total mass is below $100M_{\odot}$, and for any $\mathrm{SNR}^{\mathrm{eff}} < 19$ when the total mass is below $200M_{\odot}$. These upper bounds of the $\mathrm{SNR}^{\mathrm{eff}}$ may not seem impressive at the first sight. However, there is a significant improvement if we compare them with the upper bounds obtained when only the EOB (2, 2) mode is used which are also shown in Fig. 15. Note that the right vertical axis in Fig. 15 shows $\|\delta h\|/\|h\|$. Once the EOB and NR waveforms are aligned at low frequency, we do not allow further time or phase shift in calculating $\delta h$. This differs from the practice of Refs. [51,59] which plot $\|\delta h\|/\|h\|$ minimized over time and phase shifts.

In the $q = 6$ case, the upper-bound SNRs are lower, because of the larger error in modeling the higher-order

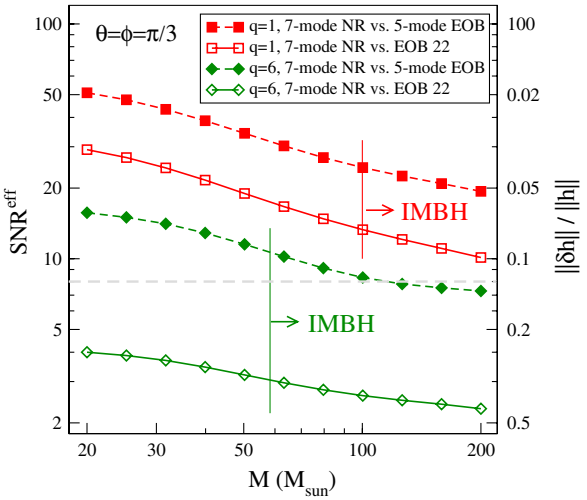


FIG. 15 (color online). The upper bound $\mathrm{SNR}^{\mathrm{eff}} \equiv \mathrm{SNR}\epsilon$ from the measurement accuracy requirement (46) versus binary total mass for $q = 1$ and 6 using Advanced LIGO noise curve. For any $\mathrm{SNR}^{\mathrm{eff}}$ below the curves, the EOB polarizations are accurate enough to avoid a systematic bias that is larger than statistical errors when estimating the binary parameters. The horizontal line indicates the single detector SNR for Advanced LIGO which is 8. The two vertical lines represent the maximum total mass for stellar-mass binary black holes with maximum black-hole mass of $50M_{\odot}$ and $q = 1$ and $q = 6$. The range of total masses on the right of those vertical lines refer to intermediate-mass black-hole binaries. The vertical axis on the right shows $\|\delta h\|/\|h\|$.

modes and the relatively high contribution to the SNR from higher-order modes for such an asymmetric binary. For stellar-mass black holes, $M \lesssim 58.3M_{\odot}$, the 5-mode EOB polarizations are accurate for $\mathrm{SNR}^{\mathrm{eff}} < 10$, and when the total mass is below $200M_{\odot}$, the 5-mode EOB polarizations are accurate for $\mathrm{SNR}^{\mathrm{eff}} < 5$. The higher-order modes in the EOB model, especially their ringdown part, clearly needs better modeling. Nevertheless, the improvement from using only the EOB (2, 2) mode as templates is significant.

In closing, we mention a few important caveats of our analysis: First, all norms and mismatches computed for Figs. 13–15 are performed only over those frequencies for which numerical data are available. At lower total mass, more gravitational-wave cycles lie in the LIGO frequency band, so this restriction becomes more severe. Therefore, at low masses, our analysis might yield an increasingly overoptimistic view.

On the other hand, the requirement (46) on the accuracy measurement may be unnecessarily stringent. In fact, although Fig. 15 would say that for certain mass ratios and total masses, the EOB waveforms will introduce biases in the binary parameters, these biases may affect binary parameters that have little astrophysical relevance—for example, the gravitational-wave phase at coalescence.

Finally, we emphasize again that the results in this section are just a first step into the problem of including higher-order modes, since we investigated only one geometrical configuration. A comprehensive investigation of the gain in effectualness and measurement accuracy, as well as the impact on estimating the source parameters, when including these rather accurate higher-order modes will be presented in a separate paper.

## V. RELATION TO PREVIOUS WORK

The EOB model we consider here differs from the nonspinning EOB model employed by Buonanno *et al.* [23] in the handling of the radiation-reaction sector. Reference [23] adopted a Padé-resummed radiation-reaction force and energy flux [22,75], while here we adopt the factorized-waveform energy flux of Refs. [26,30,76]. References [25,26] found that when generalizing the Padé-resummed flux to the spin case the agreement with the numerical energy flux is not very satisfactory. Thus, we concluded that the nonspinning EOB model with Padé-resummed flux is not a very good candidate for the generic spin EOB model.

By using the SPEC numerical merger (2, 2) mode with mass ratio $q = 1$, and inspiral (2, 2) mode with $q = 2, 3$, Buonanno *et al.* [23] calibrated the 4PN parameter in the EOB radial potential $A(r)$ and the parameter $v_{\mathrm{pole}}$ in the Padé-resummed energy flux, such that the EOB model could be also used outside the range of binary masses employed to calibrate it. We find that when comparing to the SPEC merger (2, 2) mode of this paper with mass ratios $q = 1, 2, 3$, the EOB (2, 2) mode of Ref. [23] have

maximum phase difference until merger of 0.12, 0.22, and 0.09 rad, respectively. In contrast, the model calibrated here results in smaller or comparable phase differences of 0.04, 0.08 and 0.12 rad, respectively. Numerical data for $q = 4$, 6 were not available for the calibration in Ref. [23]. Comparing the new numerical data available now with the model from Ref. [23], we find phase differences of 0.43 and 1.8 rad, respectively, for $q = 4$ and 6 (in contrast, our new model results in 0.12 and 0.15 rad, respectively; see Fig. 7). Those phase differences are obtained by using the low-frequency alignment procedure of Eq. (34). If we were adopting the two-pinching frequency procedure of Ref. [31], we would obtain 0.065 rad with pinching frequencies $M\Omega = 0.052$ and $= 0.3$ for $q = 4$, and 0.18 rad with pinching frequencies $M\Omega = 0.056$ and $= 0.15$ for $q = 6$.

Before calibration, the radiation-reaction sector of the EOB model used here almost coincides[9] with the nonspinning EOB model used in Damour and Nagar [31] in the radiation-reaction sector, but only in its uncalibrated version. In fact, the adjustable parameters used here differ from the ones used in Ref. [31]. Moreover, in this paper we also introduce adjustable parameters in the phase of some of the $(\ell, m)$ modes, and in some cases also in the factorized amplitude. Furthermore, we also modify the leading Newtonian term for the (2, 1) and (4, 4) modes [see Eq. (17)].

By using the SPEC numerical-relativity merger (2, 2) mode with mass ratio $q = 1$, and merger (2, 2) mode with $q = 2$, 4 from the Jena numerical-relativity group, Damour and Nagar [31] calibrated the 4PN and 5PN parameters in the radial potential $A(r)$. We find that when comparing to the SPEC (2, 2) modes of this paper with mass ratios $q = 1$, 2, 4, the EOB (2, 2) mode of Ref. [31] has maximum phase difference until merger of 0.25 rad, 0.36 rad, 1.32 rad, respectively, when aligning at low frequency and 0.05 rad, 0.11 rad, 0.25 rad when using the two-frequency pinching procedure. In the case of mass ratios $q = 3$ and 6 where numerical waveforms were not available for calibration, the phase differences increase to 0.93 rad and 2.3 rad, respectively, when aligning at low frequency and 0.17 rad, 0.65 rad, when using the two-frequency pinching procedure.

[9]Whereas we use the factorized waveforms with $\rho_{\ell m}$, Ref. [31] employs factorized waveforms where $(\rho_{22})^2$ is traded with its Taylor-expanded form and then Padé-resummed [30]. In the factorized waveforms, Ref. [31] also adopts a different value for the constant in the tail term $r_0 = 2$, a different odd-parity source term $\hat{S}^{(1)}_{\rm eff}(r, p_{r_*}, p_\Phi) = p_\Phi \Omega / v_\Omega^2$, and a different $N_{\ell m}$ given in Eq. (5) of Ref. [31]. Furthermore, while we include radiation-reaction force in Eq. (10c), i.e., in the equation of motion of $p_{r_*}$, Ref. [31] does not. Finally, Ref. [31] trades the Keplerian velocity with the non-Keplerian velocity in $T_{\ell m}$, $\rho_{\ell m}$ but not $\delta_{\ell m}$, and does not include the higher-order PN terms computed in Ref. [26].

We notice that once we have calibrated the EOB model to a set of numerical-relativity waveforms using the low-frequency alignment procedure of Eq. (34), the phase difference with numerical-relativity waveforms is not sensitive to the alignment method—for example, we find the same phase differences when using the two-pinching frequency procedure. By contrast, EOB waveforms calibrated with the two-frequency pinching procedure do not have the same phase difference with numerical-relativity waveforms when aligning them at low frequency. We deduce then that the low-frequency alignment procedure is more robust.

Recently, the LIGO/Virgo detectors have completed the first search for gravitational waves from high-mass black holes using analytical inspiral, merger and ringdown templates [33]. They employed the EOB model calibrated to numerical waveforms from NASA-Goddard of Ref. [20]. The mismatches between the EOB and NASA-Goddard waveforms computed in Ref. [20] are less than 3% when the total mass is $25$–$99 M_\odot$, which is the mass range used in the LIGO/Virgo search [33]. These mismatches were derived maximizing only on the time and phase, but not on the binary parameters. We find that when comparing the EOB (2, 2) mode of Ref. [20] with the EOB model developed in this paper, the phase and amplitude differences at merger are at most of 5 rad and 20%, respectively, when $q = 1$, 2, 3, 4, and 5.8 rad for $q = 6$. The EOB higher-order modes (2, 1), (3, 3), and (4, 4) were also calibrated for the first time in Ref. [20] using the NASA-Goddard numerical waveforms. In this case the matching between the inspiral-plunge and merger-ringdown waveforms was chosen at the same point in time for all the modes. Those higher-order modes were not employed in the search of Ref. [33].

## VI. CONCLUSIONS

The first search for gravitational waves from nonspinning high-mass binary black holes ($M = 25$–$99 M_\odot$) with LIGO and Virgo detectors has been recently completed, setting astrophysically meaningful upper limits [33]. The search has used for the first time templates which include inspiral, merger and ringdown. Those templates were built by combining numerical-relativity and analytical-relativity results, either through the EOB waveforms of Ref. [20] (see also the most recent improvements in Refs. [23,25,28,29,31,32]) or the phenomenological merger-ringdown waveforms proposed in Refs. [77] (see also Ref. [78] for an updated version).

In this paper we have built on Refs. [19,20,23,25,28–31], and have improved further the EOB model taking advantage of highly accurate numerical-relativity simulations with mass ratios $q = 1$, 2, 3, 4, 6 from the Caltech-Cornell-CITA collaboration [41].

By extracting several numerical-relativity quantities, such as the mode's amplitude and its second time derivative at the peak, as well as the frequency and its first

time derivative at the peak, we have improved the agreement of numerical and EOB phase and amplitude very close to merger, reproducing important features of the numerical simulations—for example, the fact that whereas the (2, 2) mode peaks at the same position of the EOB light ring, the higher-order modes peak at late times [20,32,51–53,60].

We have found that the (2, 2) mode can be calibrated with $\mathcal{M} \leq 0.1\%$ for $M = 20$–$200M_\odot$ and mass ratios $q = 1, 2, 3, 4, 6$, using only three EOB adjustable parameters, notably the 4PN and 5PN terms, $a_5$ and $a_6$, in the radial EOB potential, and the width of the comb, $\Delta t^{22}_{\rm match}$ (see Table I). We have also found that the strongest subdominant modes (2, 1), (3, 3), (4, 4) and (5, 5), can be successfully calibrated by including for each mode four EOB adjustable parameters, specifically the 3PN terms in $\rho_{21}$, $\rho_{33}$, $\rho_{44}$, $\rho_{55}$, the 2.5PN or 3.5PN terms in $\delta_{21}$, $\delta_{33}$, $\delta_{44}$ and $\delta_{55}$, the width of the comb $\Delta t^{21}_{\rm match}$, $\Delta t^{33}_{\rm match}$, $\Delta t^{44}_{\rm match}$, $\Delta t^{55}_{\rm match}$, and, in some cases, a pseudo QNM (see Table I). The reason for introducing more parameters for higher modes rests on the fact that those modes are known at PN orders lower than the (2, 2) mode. Furthermore, to achieve this very good agreement of the modes' phase and amplitude we have also used the information from numerical relativity about the peak's amplitude and frequency of Table II, and the final masses and spins of Eq. (29). These data determine the complex amplitudes entering the merger-ringdown waveform (28), and the NQC coefficients in Eq. (22).

When investigating the effectualness for detection purposes, we have found that the numerical-relativity polarizations containing the strongest seven modes have a maximum mismatch of 7% for stellar-mass binaries, and 10% for intermediate-mass binaries, when only the EOB (2, 2) mode is included for $q = 1, 2, 3, 4, 6$ and binary total masses 20–200 Hz. However, the mismatches decrease when all the four subleading EOB modes calibrated in this paper are taken into account reaching an upper bound of 0.5% for stellar-mass binaries, and 0.08% for intermediate-mass binaries. Event rates or horizon distances can be substantially increased, especially for high total masses, if those subleading modes were included in gravitational-wave searches [33].

We have also emphasized that when computing the mismatches, we do not attach any PN waveforms to the numerical-relativity waveforms, because we do not want to introduce any error due to the procedure of building hybrid PN–numerical waveforms. Moreover, for binaries with low total mass—say $20$–$100M_\odot$—many more gravitational-wave cycles than the ones of the numerical simulations used in this paper are in band. Our mismatches do not take into account these missing cycles. As a consequence if the EOB model were used to search for signals of length larger than the one of the numerical waveforms employed here, the mismatches could become larger.

We have also studied the measurement accuracy of the EOB model using the accuracy requirement proposed in Ref. [74]. Using one single Advanced LIGO detector, we have determined the SNRs below which the EOB polarizations are accurate enough that systematic biases are smaller than statistical errors. Unlike the well known fact that good phase agreement is sufficient for obtaining good effectualness, to get high upper-bound SNRs, both the amplitude and the phase of the templates must agree very well with those of the exact waveforms. Since higher-order modes have non-negligible contribution for large mass ratios, and those modes have the largest amplitude errors, we have found that the upper-bound SNRs are lower for the most asymmetric systems. We stress again the relevance of modeling the higher-order modes, because using only the (2, 2) mode would decrease significantly the upper-bound SNRs. However, it is worth noting that the accuracy requirement that we used may be too stringent since by itself it does not say which of the binary parameters is going to have biases [79]. It could turn out that the biased parameters have little relevance in astrophysics or tests of general relativity.

Finally, we have used rather long numerical-relativity waveforms, in particular, the case $q = 6$ has 40 gravitational-wave cycles before merger. Confirming previous studies [21,59,69–72] we have found, that especially for large mass ratios, the addition of more cycles at low frequency *does* affect the accuracy of the EOB waveforms (as any other PN waveforms) which were calibrated to a shorter number of cycles. So, we had to recalibrate the EOB adjustable parameters to achieve very small phase errors around merger. This recalibration is crucial for parameter estimation, but not for detection, and we expect to do it again in the future when longer or more accurate numerical-relativity waveforms for asymmetric systems will become available. Moreover, we plan to improve the matching procedure from inspiral-plunge to merger-ringdown, since the majority of the phase and amplitude error is accumulated during this transition, especially for higher-order modes. Of course, further improvement of the EOB higher-order modes also depends on the availability of sufficiently accurate numerical-relativity data especially during the last stages of inspiral, merger and ringdown.

## ACKNOWLEDGMENTS

We thank Enrico Barausse and Andrea Taracchini for useful discussions, and Ben Lackey and Cole Miller for informative interactions. A. B. and Y. P. acknowledge support from NSF Grant No. PHY-0903631. A. B. also acknowledges support from NASA Grant No. NNX09AI81G. M. B., L. B., L. K., H. P., and M. S. are supported in part by grants from the Sherman Fairchild Foundation to Caltech and Cornell, and from the Brinson

Foundation to Caltech; by NSF Grants No. PHY-0601459 and No. PHY-0652995 at Caltech; by NASA Grant No. NNX09AF97G at Caltech; by NSF Grants No. PHY-0652952 and No. PHY-0652929 at Cornell; and by NASA Grant No. NNX09AF96G at Cornell. H. P. gratefully acknowledges support from the NSERC of Canada , from Canada Research Chairs Program, and from the Canadian Institute for Advanced Research.

## APPENDIX A: THE $(\ell, m) = (3, 2)$ MODE

Reference [19] found that the numerical-relativity (3, 2) mode contains QNMs with $(\ell, m) = (3, 2)$ and $(\ell, m) = (2, 2)$. This beating of QNMs with the same $m$ but different $\ell$ arises in the transformation from the spin-weighted spheroidal harmonics (which are eigenmodes of the radiation generated by the perturbed final black hole) to the spin-weighted spherical harmonics that are used to decompose the multipolar waveform. This is a general feature of modes with $\ell > 2$ and $m < \ell$, and since the (3, 2) mode is the dominant one among such modes, we discuss its modeling and possible calibration in this section.

First, we confirm the result of Ref. [19] that the ringdown portion of the (3, 2) mode can be accurately modeled by a linear superposition of QNMs with both $(\ell, m) = (3, 2)$ and $(\ell, m) = (2, 2)$ modes. The result of Ref. [19] was restricted to the equal-mass case. Here we extend this analysis to unequal masses and add more overtones. We fit the numerical ringdown mode with either (i) a set of eight QNMs with $(\ell = 3, m = 2, n = 0, 1, \ldots, 7)$ or (ii) a set of eight QNMs with $(\ell = 3, m = 2, n = 0, 1, \ldots, 4)$ and $(\ell = 3, m = 2, n = 0, 1, 2)$. For mass ratios $q = 1$ and 6, we compare the fitting results with numerical waveforms in Fig. 16. The results for other mass ratios are similar. The very different performance of sets (i) and (ii) shows clearly that the numerical ringdown mode does contain contributions from $(\ell, m) = (2, 2)$ QNMs.

Second, for the case $q = 6$, we explore in Fig. 17 the possibility of modeling the numerical ringdown (3, 2) mode as a linear superposition of the QNMs of set (ii), using the EOB matching procedure of Sec. II C. We observe that although the beating of the $(\ell, m) = (3, 2)$ and $(\ell, m) = (2, 2)$ QNMs reproduce qualitatively well the oscillations in the ringdown amplitude and frequency, the behavior of the two curves "NR" and "NR + QNM" is very different. Therefore, we deduce that the current matching procedure, which uses the information of a small segment of inspiral-plunge waveform before the peak of the amplitude, does not provide us with the correct QNMs coefficients when different $\ell$ values are present. Since this matching procedure is applied to build the calibrated EOB modes, we find that the same problem affects the calibration of the EOB (3, 2) mode. We postpone to the future the solution to this important issue.

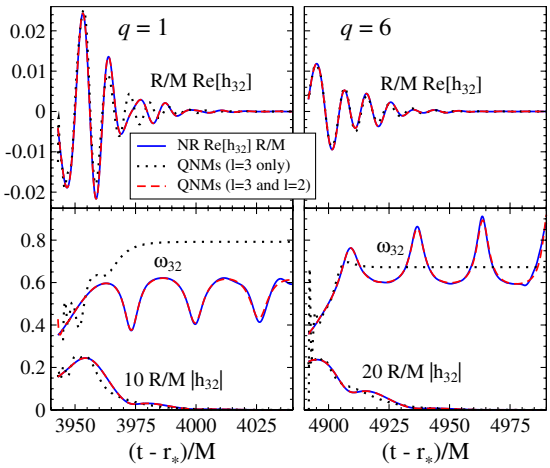


FIG. 16 (color online). Investigation of the (3, 2) mode during ringdown for $q = 1$ and 6. The top panels show the mode itself, and the lower panels split the mode into amplitude and frequency. The continuous lines represent the numerical-relativity modes. The dotted lines are a fit to eight QNM modes of $(\ell = 3, m = 2, n = 0, 1, \ldots, 7)$. The dashed lines are a fit to eight QNMs of $(\ell = 3, m = 2, n = 0, 1, \ldots, 4)$ and $(\ell = 2, m = 2, n = 0, 1, 2)$. The horizontal axis is the retarded time in the numerical-relativity simulation.

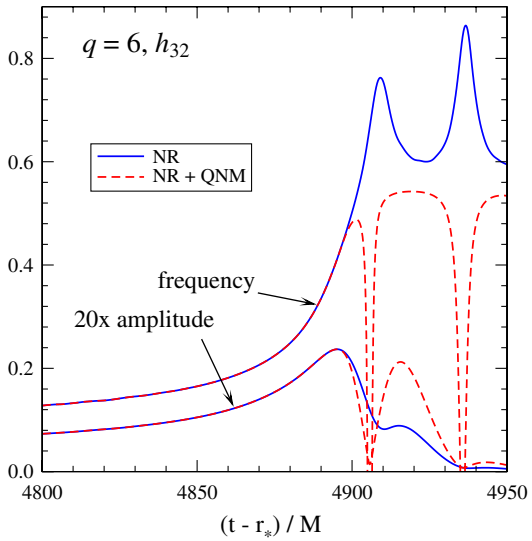


FIG. 17 (color online). Amplitude and frequency comparisons between full NR (3, 2) mode and "NR + QNM" (3, 2) mode generated by attaching the QNMs to the inspiral-plunge numerical waveform. The "NR + QNM" waveform is generated by attaching the following set of eight QNMs $(\ell = 3, m = 2, n = 0, 1, \ldots, 4)$ and $(\ell = 2, m = 2, n = 0, 1, 2)$. Note that the amplitudes have been multiplied by a factor of 20, so that they are more visible. The horizontal axis is the retarded time in the numerical-relativity simulation.

## APPENDIX B: QUANTITIES ENTERING THE EOB GRAVITATIONAL MODES

Following Ref. [30], we introduce the velocity parameter, $\bar{v} \equiv (\Omega H^{\rm real})^{1/3}$. The explicit expressions of the function $\delta_{\ell m}$ then read [26,30]

$$\delta_{22} = \frac{7}{3}\bar{v}^3 + \frac{428}{105}\pi\bar{v}^6 + \left(\frac{1712}{315}\pi^2 - \frac{2203}{81}\right)\bar{v}^9 - 24\nu v_\Omega^5, \tag{B1a}$$

$$\delta_{21} = \frac{2}{3}\bar{v}^3 + \frac{107}{105}\pi\bar{v}^6 + \left(\frac{214}{315}\pi^2 - \frac{272}{81}\right)\bar{v}^9 - \frac{493}{42}\nu \times v_\Omega^5 + \delta_{21}^{(7)}\nu v_\Omega^7, \tag{B1b}$$

$$\delta_{33} = \frac{13}{10}\bar{v}^3 + \frac{39}{7}\pi\bar{v}^6 + \left(\frac{78}{7}\pi^2 - \frac{227827}{3000}\right)\bar{v}^9 - \frac{80897}{2430}\nu \times v_\Omega^5 + \delta_{33}^{(7)}\nu v_\Omega^7, \tag{B2a}$$

$$\delta_{32} = \frac{10 + 33\nu}{15(1-3\nu)}\bar{v}^3 + \frac{52}{21}\pi\bar{v}^6 + \left(\frac{208}{63}\pi^2 - \frac{9112}{405}\right)\bar{v}^9, \tag{B2b}$$

$$\delta_{31} = \frac{13}{30}\bar{v}^3 + \frac{13}{21}\pi\bar{v}^6 + \left(\frac{26}{63}\pi^2 - \frac{227827}{81000}\right)\bar{v}^9 - \frac{17\nu}{10}v_\Omega^5, \tag{B2c}$$

$$\delta_{44} = \frac{112 + 219\nu}{120(1-3\nu)}\bar{v}^3 + \frac{25136}{3465}\pi\bar{v}^6 + \delta_{44}^{(5)}\nu v_\Omega^5, \tag{B3a}$$

$$\delta_{43} = \frac{486 + 4961\nu}{810(1-2\nu)}\bar{v}^3 + \frac{1571}{385}\pi\bar{v}^6, \tag{B3b}$$

$$\delta_{42} = \frac{7(1+6\nu)}{15(1-3\nu)}\bar{v}^3 + \frac{6284}{3465}\pi\bar{v}^6, \tag{B3c}$$

$$\delta_{41} = \frac{2 + 507\nu}{10(1-2\nu)}\bar{v}^3 + \frac{1571}{3465}\pi v^6, \tag{B3d}$$

$$\delta_{55} = \frac{96875 + 857528\nu}{131250(1-2\nu)}\bar{v}^3 + \delta_{55}^{(5)}\nu v_\Omega^5, \tag{B4a}$$

$$\delta_{54} = \frac{8}{15}\bar{v}^3, \tag{B4b}$$

$$\delta_{53} = \frac{31}{70}\bar{v}^3, \tag{B4c}$$

$$\delta_{52} = \frac{4}{15}\bar{v}^3, \tag{B4d}$$

$$\delta_{51} = \frac{31}{210}\bar{v}^3, \tag{B4e}$$

$$\delta_{66} = \frac{43}{70}\bar{v}^3, \tag{B5a}$$

$$\delta_{65} = \frac{10}{21}\bar{v}^3, \tag{B5b}$$

$$\delta_{64} = \frac{43}{105}\bar{v}^3, \tag{B5c}$$

$$\delta_{63} = \frac{2}{7}\bar{v}^3, \tag{B5d}$$

$$\delta_{62} = \frac{43}{210}\bar{v}^3, \tag{B5e}$$

$$\delta_{61} = \frac{2}{21}\bar{v}^3, \tag{B5f}$$

$$\delta_{77} = \frac{19}{36}\bar{v}^3, \tag{B6a}$$

$$\delta_{75} = \frac{95}{252}\bar{v}^3, \tag{B6b}$$

$$\delta_{73} = \frac{19}{84}\bar{v}^3, \tag{B6c}$$

$$\delta_{71} = \frac{19}{252}\bar{v}^3. \tag{B6d}$$

Note that the 2.5PN and 3.5PN coefficients $\delta_{21}^{(5)}$, $\delta_{33}^{(7)}$ and $\delta_{44}^{(7)}$ in Eqs. (B1b), (B2a), and (B3a) are not known in PN theory. They are determined by calibrating the EOB to numerical-relativity waveforms. Their explicit expressions for these parameters are given by Eq. (39).

The following quantities enter the Newtonian modes in Eq. (16)

$$n_{\ell m}^{(0)} = (im)^\ell \frac{8\pi}{(2\ell+1)!!}\sqrt{\frac{(\ell+1)(\ell+2)}{\ell(\ell-1)}}, \tag{B7a}$$

$$n_{\ell m}^{(1)} = -(im)^\ell \frac{16\pi i}{(2\ell+1)!!}\sqrt{\frac{(2\ell+1)(\ell+2)(\ell^2-m^2)}{(2\ell-1)(\ell+1)\ell(\ell-1)}}, \tag{B7b}$$

and

$$c_{\ell+\epsilon}(\nu) = \left(\frac{1}{2} - \frac{1}{2}\sqrt{1-4\nu}\right)^{\ell+\epsilon-1} + (-1)^{\ell+\epsilon}\left(\frac{1}{2} + \frac{1}{2}\sqrt{1-4\nu}\right)^{\ell+\epsilon-1}. \tag{B8}$$

The odd-parity modes $\rho_{\ell m}^L$ and even-parity modes $\rho_{\ell m}$ read [26,30]

$$\rho_{22} = 1 + \left(\frac{55\nu}{84} - \frac{43}{42}\right)v_\Omega^2 + \left(\frac{19583\nu^2}{42336} - \frac{33025\nu}{21168} - \frac{20555}{10584}\right)v_\Omega^4 + \left(\frac{10620745\nu^3}{39118464} - \frac{6292061\nu^2}{3259872} + \frac{41\pi^2\nu}{192} - \frac{48993925\nu}{9779616} - \frac{428\,\mathrm{eulerlog}_2(v_\Omega^2)}{105} + \frac{1556919113}{122245200}\right)v_\Omega^6 + \left(\frac{9202\,\mathrm{eulerlog}_2(v_\Omega^2)}{2205} - \frac{387216563023}{160190110080}\right)v_\Omega^8 + \left(\frac{439877\,\mathrm{eulerlog}_2(v_\Omega^2)}{55566} - \frac{16094530514677}{533967033600}\right)v_\Omega^{10}, \tag{B9a}$$

$$\rho_{21}^L = 1 + \left(\frac{23\nu}{84} - \frac{59}{56}\right)v_\Omega^2 + \left(\frac{617\nu^2}{4704} - \frac{10993\nu}{14112} - \frac{47009}{56448}\right)v_\Omega^4 + \left(\frac{7613184941}{2607897600} - \frac{107\,\mathrm{eulerlog}_1(v_\Omega^2)}{105}\right)v_\Omega^6 + \rho_{21}^{(6)}\nu v_\Omega^6 + \left(\frac{6313\,\mathrm{eulerlog}_1(v_\Omega^2)}{5880} - \frac{1168617463883}{911303737344}\right)v_\Omega^8 + \left(\frac{5029963\,\mathrm{eulerlog}_1(v_\Omega^2)}{5927040} - \frac{63735873771463}{16569158860800}\right)v_\Omega^{10}, \tag{B9b}$$

$$\rho_{33} = 1 + \left(\frac{2\nu}{3} - \frac{7}{6}\right)v_\Omega^2 + \left(\frac{149\nu^2}{330} - \frac{1861\nu}{990} - \frac{6719}{3960}\right)v_\Omega^4 + \left(\frac{3203101567}{227026800} - \frac{26\,\mathrm{eulerlog}_3(v_\Omega^2)}{7}\right)v_\Omega^6 + \rho_{33}^{(6)}\nu v_\Omega^6 + \left(\frac{13\,\mathrm{eulerlog}_3(v_\Omega^2)}{3} - \frac{57566572157}{8562153600}\right)v_\Omega^8, \tag{B10a}$$

$$\rho_{32}^L = 1 + \frac{320\nu^2 - 1115\nu + 328}{270(3\nu - 1)}v_\Omega^2 + \frac{3085640\nu^4 - 20338960\nu^3 - 4725605\nu^2 + 8050045\nu - 1444528}{1603800(1 - 3\nu)^2}v_\Omega^4 + \left(\frac{5849948554}{940355325} - \frac{104\,\mathrm{eulerlog}_2(v_\Omega^2)}{63}\right)v_\Omega^6 + \left(\frac{17056\,\mathrm{eulerlog}_2(v_\Omega^2)}{8505} - \frac{10607269449358}{3072140846775}\right)v_\Omega^8, \tag{B10b}$$

$$\rho_{31} = 1 - \left(\frac{2\nu}{9} + \frac{13}{18}\right)v_\Omega^2 + \left(-\frac{829\nu^2}{1782} - \frac{1685\nu}{1782} + \frac{101}{7128}\right)v_\Omega^4 + \left(\frac{11706720301}{6129723600} - \frac{26\,\mathrm{eulerlog}_1(v_\Omega^2)}{63}\right)v_\Omega^6 + \left(\frac{169\,\mathrm{eulerlog}_1(v_\Omega^2)}{567} + \frac{2606097992581}{4854741091200}\right)v_\Omega^8. \tag{B10c}$$

$$\rho_{44} = 1 + \frac{2625\nu^2 - 5870\nu + 1614}{1320(3\nu - 1)}v_\Omega^2 + \frac{1252563795\nu^4 - 6733146000\nu^3 - 313857376\nu^2 + 2338945704\nu - 511573572}{317116800(1 - 3\nu)^2}v_\Omega^4 + \left(\frac{16600939332793}{1098809712000} - \frac{12568\,\mathrm{eulerlog}_4(v_\Omega^2)}{3465}\right)v_\Omega^6 + \rho_{44}^{(6)}\nu v_\Omega^6, \tag{B11a}$$

$$\rho_{43}^L = 1 + \frac{160\nu^2 - 547\nu + 222}{176(2\nu - 1)}v_\Omega^2 - \frac{6894273}{7047040}v_\Omega^4 + \left(\frac{1664224207351}{195343948800} - \frac{1571\,\mathrm{eulerlog}_3(v_\Omega^2)}{770}\right)v_\Omega^6, \tag{B11b}$$

$$\rho_{42} = 1 + \frac{285\nu^2 - 3530\nu + 1146}{1320(3\nu - 1)}v_\Omega^2 + \frac{-379526805\nu^4 - 3047981160\nu^3 + 1204388696\nu^2 + 295834536\nu - 114859044}{317116800(1 - 3\nu)^2}v_\Omega^4 + \left(\frac{848238724511}{219761942400} - \frac{3142\,\mathrm{eulerlog}_2(v_\Omega^2)}{3465}\right)v_\Omega^6, \tag{B11c}$$

$$\rho_{41}^L = 1 + \frac{288\nu^2 - 1385\nu + 602}{528(2\nu - 1)}v_\Omega^2 - \frac{7775491}{21141120}v_\Omega^4 + \left(\frac{1227423222031}{1758095539200} - \frac{1571\,\mathrm{eulerlog}_1(v_\Omega^2)}{6930}\right)v_\Omega^6. \tag{B11d}$$

$$\rho_{55} = 1 + \frac{512\nu^2 - 1298\nu + 487}{390(2\nu - 1)} v_\Omega^2 - \frac{3353747}{2129400} v_\Omega^4 + \rho_{55}^{(6)} \nu v_\Omega^6, \tag{B12a}$$

$$\rho_{54}^L = 1 + \frac{33320\nu^3 - 127610\nu^2 + 96019\nu - 17448}{13650(5\nu^2 - 5\nu + 1)} v_\Omega^2 - \frac{16213384}{15526875} v_\Omega^4, \tag{B12b}$$

$$\rho_{53} = 1 + \frac{176\nu^2 - 850\nu + 375}{390(2\nu - 1)} v_\Omega^2 - \frac{410833}{709800} v_\Omega^4, \tag{B12c}$$

$$\rho_{52}^L = 1 + \frac{21980\nu^3 - 104930\nu^2 + 84679\nu - 15828}{13650(5\nu^2 - 5\nu + 1)} v_\Omega^2 - \frac{7187914}{15526875} v_\Omega^4, \tag{B12d}$$

$$\rho_{51} = 1 + \frac{8\nu^2 - 626\nu + 319}{390(2\nu - 1)} v_\Omega^2 - \frac{31877}{304200} v_\Omega^4. \tag{B12e}$$

$$\rho_{66} = 1 + \frac{273\nu^3 - 861\nu^2 + 602\nu - 106}{84(5\nu^2 - 5\nu + 1)} v_\Omega^2 - \frac{1025435}{659736} v_\Omega^4, \tag{B13a}$$

$$\rho_{65}^L = 1 + \frac{220\nu^3 - 910\nu^2 + 838\nu - 185}{144(3\nu^2 - 4\nu + 1)} v_\Omega^2, \tag{B13b}$$

$$\rho_{64} = 1 + \frac{133\nu^3 - 581\nu^2 + 462\nu - 86}{84(5\nu^2 - 5\nu + 1)} v_\Omega^2 - \frac{476887}{659736} v_\Omega^4, \tag{B13c}$$

$$\rho_{63}^L = 1 + \frac{156\nu^3 - 750\nu^2 + 742\nu - 169}{144(3\nu^2 - 4\nu + 1)} v_\Omega^2, \tag{B13d}$$

$$\rho_{62} = 1 + \frac{49\nu^3 - 413\nu^2 + 378\nu - 74}{84(5\nu^2 - 5\nu + 1)} v_\Omega^2 - \frac{817991}{3298680} v_\Omega^4, \tag{B13e}$$

$$\rho_{61}^L = 1 + \frac{124\nu^3 - 670\nu^2 + 694\nu - 161}{144(3\nu^2 - 4\nu + 1)} v_\Omega^2, \tag{B13f}$$

$$\rho_{77} = 1 + \frac{1380\nu^3 - 4963\nu^2 + 4246\nu - 906}{714(3\nu^2 - 4\nu + 1)} v_\Omega^2, \tag{B14a}$$

$$\rho_{76}^L = 1 + \frac{6104\nu^4 - 29351\nu^3 + 37828\nu^2 - 16185\nu + 2144}{1666(7\nu^3 - 14\nu^2 + 7\nu - 1)} v_\Omega^2, \tag{B14b}$$

$$\rho_{75} = 1 + \frac{804\nu^3 - 3523\nu^2 + 3382\nu - 762}{714(3\nu^2 - 4\nu + 1)} v_\Omega^2, \tag{B14c}$$

$$\rho_{74}^L = 1 + \frac{41076\nu^4 - 217959\nu^3 + 298872\nu^2 - 131805\nu + 17756}{14994(7\nu^3 - 14\nu^2 + 7\nu - 1)} v_\Omega^2, \tag{B14d}$$

$$\rho_{73} = 1 + \frac{420\nu^3 - 2563\nu^2 + 2806\nu - 666}{714(3\nu^2 - 4\nu + 1)} v_\Omega^2, \tag{B14e}$$

$$\rho_{72}^L = 1 + \frac{32760\nu^4 - 190239\nu^3 + 273924\nu^2 - 123489\nu + 16832}{14994(7\nu^3 - 14\nu^2 + 7\nu - 1)} v_\Omega^2, \tag{B14f}$$

$$\rho_{71} = 1 + \frac{228\nu^3 - 2083\nu^2 + 2518\nu - 618}{714(3\nu^2 - 4\nu + 1)} v_\Omega^2. \tag{B14g}$$

Here we use $\text{eulerlog}_m(v_\Omega^2) = \gamma_E + \log 2 + \log m + 1/2 \log v_\Omega^2$, with $\gamma_E$ being the Euler constant. Note that the 3PN coefficients $\rho_{21}^{(6)}$, $\rho_{33}^{(6)}$ and $\rho_{44}^{(6)}$ in Eqs. (B9b), (B10a), and (B11a) are not known in PN theory. They are determined by calibrating the EOB to numerical-relativity waveforms. The calibrated expressions are given by Eq. (38).

[1] B. Abbott *et al.* (LIGO Scientific Collaboration), Rep. Prog. Phys. **72**, 076901 (2009).
[2] F. Acernese *et al.* (Virgo Collaboration), Classical Quantum Gravity **25**, 184001 (2008).
[3] H. Grote (GEO600 Collaboration), Classical Quantum Gravity **25**, 114043 (2008).
[4] K. Kuroda (the LCGT Collaboration), Classical Quantum Gravity **27**, 084004 (2010).
[5] L. Blanchet, Living Rev. Relativity **9**, 4 (2006), http://relativity.livingreviews.org/Articles/lrr-2006-4/.
[6] M. Sasaki and H. Tagoshi, Living Rev. Relativity **6**, 6 (2003), http://relativity.livingreviews.org/Articles/lrr-2003-6/.
[7] T. Futamase and Y. Itoh, Living Rev. Relativity **10**, 2 (2007), http://relativity.livingreviews.org/Articles/lrr-2007-2/.
[8] W. D. Goldberger and I. Z. Rothstein, Phys. Rev. D **73**, 104029 (2006).
[9] F. Pretorius, Phys. Rev. Lett. **95**, 121101 (2005).
[10] J. G. Baker, J. Centrella, D.-I. Choi, M. Koppitz, and J. van Meter, Phys. Rev. Lett. **96**, 111102 (2006).
[11] M. Campanelli, C. O. Lousto, P. Marronetti, and Y. Zlochower, Phys. Rev. Lett. **96**, 111101 (2006).
[12] A. Buonanno and T. Damour, Phys. Rev. D **62**, 064015 (2000).
[13] A. Buonanno and T. Damour, Phys. Rev. D **59**, 084006 (1999).
[14] T. Damour, P. Jaranowski, and G. Schäfer, Phys. Rev. D **62**, 084011 (2000).
[15] T. Damour, Phys. Rev. D **64**, 124013 (2001).
[16] A. Buonanno, Y. Chen, and T. Damour, Phys. Rev. D **74**, 104005 (2006).
[17] T. Damour, P. Jaranowski, and G. Schäfer, Phys. Rev. D **78**, 024009 (2008).
[18] E. Barausse and A. Buonanno, Phys. Rev. D **81**, 084024 (2010).
[19] A. Buonanno, G. B. Cook, and F. Pretorius, Phys. Rev. D **75**, 124018 (2007).
[20] A. Buonanno, Y. Pan, J. G. Baker, J. Centrella, B. J. Kelly, S. T. McWilliams, and J. R. van Meter, Phys. Rev. D **76**, 104049 (2007).
[21] Y. Pan, A. Buonanno, J. G. Baker, J. Centrella, B. J. Kelly, S. T. McWilliams, F. Pretorius, and J. R. van Meter, Phys. Rev. D **77**, 024014 (2008).
[22] M. Boyle, A. Buonanno, L. E. Kidder, A. H. Mroué, Y. Pan, H. P. Pfeiffer, and M. A. Scheel, Phys. Rev. D **78**, 104020 (2008).
[23] A. Buonanno, Y. Pan, H. P. Pfeiffer, M. A. Scheel, L. T. Buchman, and L. E. Kidder, Phys. Rev. D **79**, 124028 (2009).
[24] E. Racine, A. Buonanno, and L. E. Kidder, Phys. Rev. D **80**, 044010 (2009).
[25] Y. Pan, A. Buonanno, L. Buchman, T. Chu, L. Kidder, H. Pfeiffer, and M. Scheel, Phys. Rev. D **81**, 084041 (2010).
[26] Y. Pan, A. Buonanno, R. Fujita, E. Racine, and H. Tagoshi, Phys. Rev. D **83**, 064003 (2011).
[27] T. Damour and A. Nagar, Phys. Rev. D **77**, 024043 (2008).
[28] T. Damour, A. Nagar, E. N. Dorband, D. Pollney, and L. Rezzolla, Phys. Rev. D **77**, 084017 (2008).
[29] T. Damour, A. Nagar, M. Hannam, S. Husa, and B. Brügmann, Phys. Rev. D **78**, 044039 (2008).
[30] T. Damour, B. R. Iyer, and A. Nagar, Phys. Rev. D **79**, 064004 (2009).
[31] T. Damour and A. Nagar, Phys. Rev. D **79**, 081503 (2009).
[32] S. Bernuzzi, A. Nagar, and A. Zenginoglu, Phys. Rev. D **83**, 064010 (2011).
[33] J. Abadie *et al.* (LIGO Scientific Collaboration and Virgo Collaboration), Phys. Rev. D **83**, 122005 (2011).
[34] M. Scheel, M. Boyle, T. Chu, L. Kidder, K. Matthews, and H. Pfeiffer, Phys. Rev. D **79**, 024003 (2009).
[35] B. Szilagyi, L. Lindblom, and M. A. Scheel, Phys. Rev. D **80**, 124010 (2009).
[36] M. Boyle, D. A. Brown, L. E. Kidder, A. H. Mroué, H. P. Pfeiffer, M. A. Scheel, G. B. Cook, and S. A. Teukolsky, Phys. Rev. D **76**, 124038 (2007).
[37] H. P. Pfeiffer, D. A. Brown, L. E. Kidder, L. Lindblom, G. Lovelace, and M. A. Scheel, Classical Quantum Gravity **24**, S59 (2007).
[38] L. Lindblom, M. A. Scheel, L. E. Kidder, R. Owen, and O. Rinne, Classical Quantum Gravity **23**, S447 (2006).
[39] M. A. Scheel, H. P. Pfeiffer, L. Lindblom, L. E. Kidder, O. Rinne, and S. A. Teukolsky, Phys. Rev. D **74**, 104006 (2006).
[40] http://www.black-holes.org/SpEC.html.
[41] L. T. Buchman, H. P. Pfeiffer, and M. A. Scheel, "Simulations of Non-equal Mass Black Hole Binaries,"(to be published).
[42] O. Rinne, L. T. Buchman, M. A. Scheel, and H. P. Pfeiffer, Classical Quantum Gravity **26**, 075009 (2009).
[43] M. Boyle and A. H. Mroúe, Phys. Rev. D **80**, 124045 (2009).
[44] T. Damour, B. R. Iyer, P. Jaranowski, and B. S. Sathyaprakash, Phys. Rev. D **67**, 064028 (2003).
[45] T. Damour and A. Nagar, Phys. Rev. D **76**, 064028 (2007).
[46] T. Damour and A. Nagar, Phys. Rev. D **76**, 044003 (2007).
[47] T. Damour, Phys. Rev. D **81**, 024017 (2010).
[48] L. Blanchet, S. L. Detweiler, A. Le Tiec, and B. F. Whiting, Phys. Rev. D **81**, 084033 (2010).
[49] N. Yunes, A. Buonanno, S. A. Hughes, M. Coleman Miller, and Y. Pan, Phys. Rev. Lett. **104**, 091102 (2010).
[50] N. Yunes *et al.*, Phys. Rev. D **83**, 044044 (2011).
[51] J. D. Schnittman, A. Buonanno, J. R. van Meter, J. G. Baker, W. D. Boggs, J. Centrella, B. J. Kelly, and S. T. McWilliams, Phys. Rev. D **77**, 044031 (2008).
[52] J. G. Baker, W. D. Boggs, J. Centrella, B. J. Kelly, S. T. McWilliams, and J. R. van Meter, Phys. Rev. D **78**, 044046 (2008).
[53] S. Bernuzzi and A. Nagar, Phys. Rev. D **81**, 084056 (2010).
[54] T. Damour and A. Gopakumar, Phys. Rev. D **73**, 124006 (2006).
[55] E. Berti, V. Cardoso, and C. M. Will, Phys. Rev. D **73**, 064030 (2006).
[56] T. Regge and J. A. Wheeler, Phys. Rev. **108**, 1063 (1957).
[57] F. J. Zerilli, Phys. Rev. Lett. **24**, 737 (1970).
[58] O. Sarbach and M. Tiglio, Phys. Rev. D **64**, 084016 (2001).
[59] I. MacDonald, S. Nissanke, and H. P. Pfeiffer, Classical Quantum Gravity **28**, , 134002 (2011).
[60] E. Barausse, A. Buonanno, S. A. Hughes, G. Khanna, S. O'Sullivan, and Y. Pan, arXiv:1110.3081.

[61] L. Barack and N. Sago, Phys. Rev. Lett. **102**, 191101 (2009).
[62] D. Shoemaker (LIGO Collaboration), LIGO Document T0900288-v3, 2010, https://dcc.ligo.org/cgi-bin/DocDB/ShowDocument?docid=2974.
[63] D. McKechan, C. Robinson, and B. Sathyaprakash, Classical Quantum Gravity **27**, 084020 (2010).
[64] J. M. Silverman and A. V. Filippenko, Astrophys. J. Lett. **678**, L17 (2008).
[65] A. H. Prestwich, R. Kilgard, P. A. Crowther, S. Carpano, A. M. T. Pollock, A. Zezas, S. H. Saar, T. P. Roberts, and M. J. Ward, Astrophys. J. Lett. **669**, L21 (2007).
[66] K. Belczynski, T. Bulik, C. L. Fryer, A. Ruiter, F. Valsecchi, J. S. Vink, and J. R. Hurley, Astrophys. J. **714**, 1217 (2010).
[67] M. Coleman Miller and E. J. M. Colbert, Int. J. Mod. Phys. D **13**, 1 (2004).
[68] J. M. Fregeau, S. L. Larson, M. C. Miller, R. O'Shaughnessy, and F. A. Rasio, Astrophys. J. Lett. **646**, L135 (2006).
[69] A. Buonanno, B. R. Iyer, E. Ochsner, Y. Pan, and B. S. Sathyaprakash, Phys. Rev. D **80**, 084043 (2009).
[70] M. Hannam, S. Husa, F. Ohme, and P. Ajith, Phys. Rev. D **82**, 124052 (2010).
[71] T. Damour, A. Nagar, and M. Trias, Phys. Rev. D **83**, 024006 (2011).
[72] M. Boyle, Phys. Rev. D **84**, 064013 (2011).
[73] M. A. Miller, Phys. Rev. D **71**, 104016 (2005).
[74] L. Lindblom, B. J. Owen, and D. A. Brown, Phys. Rev. D **78**, 124020 (2008).
[75] T. Damour, B. R. Iyer, and B. S. Sathyaprakash, Phys. Rev. D **57**, 885 (1998).
[76] R. Fujita and B. R. Iyer, Phys. Rev. D **82**, 044051 (2010).
[77] P. Ajith, S. Babak, Y. Chen, M. Hewitson, B. Krishnan, A. M. Sintes, J. T. Whelan, B. Brügmann, P. Diener, N. Dorband, J. Gonzalez, M. Hannam, S. Husa, D. Pollney, L. Rezzolla, L. Santamaía, U. Sperhake, and J. Thornburg, Phys. Rev. D **77**, 104017 (2008).
[78] L. Santamaría, F. Ohme, P. Ajith, B. Brügmann, N. Dorband, M. Hannam, S. Husa, P. Mösta, D. Pollney, C. Reisswig, E. L. Robinson, J. Seiler, and B. Krishnan, Phys. Rev. D **82**, 064016 (2010).
[79] C. Cutler and M. Vallisneri, Phys. Rev. D **76**, 104018 (2007).